Geochemistry, Geophysics, Geosystems

RESEARCH ARTICLE
10.1029/2018GC008129

Special Section:
Magmatic and volcanic processes in continental rifts

Using Ambient Noise to Image the Northern East African Rift

Emma L. Chambers[1], Nicholas Harmon[1], Derek Keir[1,2], and Catherine A. Rychert[1]

[1]National Oceanography Centre Southampton, University of Southampton, Southampton, UK, [2]Dipartimento di Scienze della Terra, Università degli Studi di Firenze, Florence, Italy

Key Points:
- Uppermost mantle velocities are 9% slower than the ak135 model requiring elevated temperatures and fluids; melt percent estimates are 1.1-2%
- The Main Ethiopian Rift has the slowest velocities at all depths in this study due to longer melt residence times within the crust
- Shear velocity is heterogeneous beneath the northwestern plateau suggesting crustal structure, and formation is more complex than thought

Supporting Information:
- Supporting Information S1

Correspondence to:
E. L. Chambers,
e.chambers@soton.ac.uk

Citation:
Chambers, E. L., Harmon, N., Keir, D., & Rychert, C. A. (2019). Using ambient noise to image the northern East African Rift. *Geochemistry, Geophysics, Geosystems*, *20*, 2091–2109. https://doi.org/10.1029/2018GC008129

Received 6 DEC 2018
Accepted 31 MAR 2019
Accepted article online 02 APR 2019
Published online 25 APR 2019

Abstract The northern East African Rift (EAR) is a unique location where we observe continental rifting in the Main Ethiopian Rift (MER) transitioning to incipient seafloor spreading in Afar. Here we present a 3-D absolute shear wave velocity model of the crust and uppermost mantle of the northern EAR generated from ambient noise tomography. We generate 4,820 station pair correlation functions, from 170 stations (present over 12 years), which were inverted for phase velocity from 8–33 s period and finally for 3-D absolute shear velocity structure to 60-km depth. Everywhere in the uppermost mantle, shear velocity is slower than expected for a mantle peridotite composition (<4.1 km/s). This suggests the presence of pervasive partial melt, with focused upwelling and melt storage beneath the MER, where the slowest velocities (3.20 km/s ± 0.03) are observed. Average crustal shear velocity is faster beneath Afar (3.83 km/s ± 0.04) than the MER (3.60 km/s ± 0.04), albeit Afar has localized slow velocities beneath active volcanic centers. We interpret these slow-velocity regions (including the MER) as magmatic intrusions and heating of the crust. Beneath the northwestern plateau, crustal velocities are laterally heterogeneous (3.3–3.65 ± 0.05 km/s at 10 km), suggesting a complex geological history and inhomogeneous magma distribution during rift development. Comparison between the MER and Afar allows us to draw conclusions between different stages of rifting. In particular, the MER has the slowest crustal velocities, consistent with longer magma residence times in the crust, early during the breakup process.

Plain Language Summary In Ethiopia, the African Continent is rifting apart to slowly form a new ocean basin, which will expand the Red Sea and the Gulf of Aden. How and why this rifting is occurring remains an important unanswered question in earth science. We know tectonic forces are partly responsible, but magmatism also seems a key ingredient for breaking up Africa. Here we use seismic images obtained from signals pulled out of noise, to understand the crustal structure of the region; In particular, how and where magma is stored in the crust, and its relationship to the different stages of continental breakup visible in the region. We find evidence for long-term melt storage in places where rifting is just beginning in southern Ethiopia; whereas in regions where the crust is thinner due to extensive rifting, magma erupts more regularly. The long-term storage of magma in unrifted crust may help to heat and weaken it, allowing rifting to accelerate and propagate further south. We are also able to image regions with hydrothermal fluids in the shallow parts of the crust in inactive fault zones. These results provide insight into the breakup process and the role magma plays at different stages of rifting.

1. Introduction

Continents are thought to rift from a combination of tectonic and magmatic processes (Buck, 2004). Tectonic processes do not provide enough force to rift thick continental lithosphere, instead requiring emplacement of magma to rift with lower forces (Buck, 2006; Mackenzie et al., 2005). In areas of magma-assisted rifting there is debate as to the distribution of melt storage and migration pathways, and how these change through time during the rifting to breakup process (Hutchison et al., 2015; Magee et al., 2016; White et al., 2008). To better understand the processes responsible for rifting the upper lithosphere, knowledge of the crustal structure both on and off the rift is required. The rift flanks give an insight into the original crustal structure, while variations within the rift give clues to the importance of melt at different stages of rifting.

The Northern East African Rift (EAR) is the archetypal example of magma-assisted rifting where the transition from continental rifting to seafloor spreading is observed within Ethiopia. The early stages of rifting are observed in the Main Ethiopian Rift (MER), with rifting becoming more evolved from south to north (Ebinger & Casey, 2001; WoldeGabriel et al., 1990). Afar is the end member of the EAR, transitioning

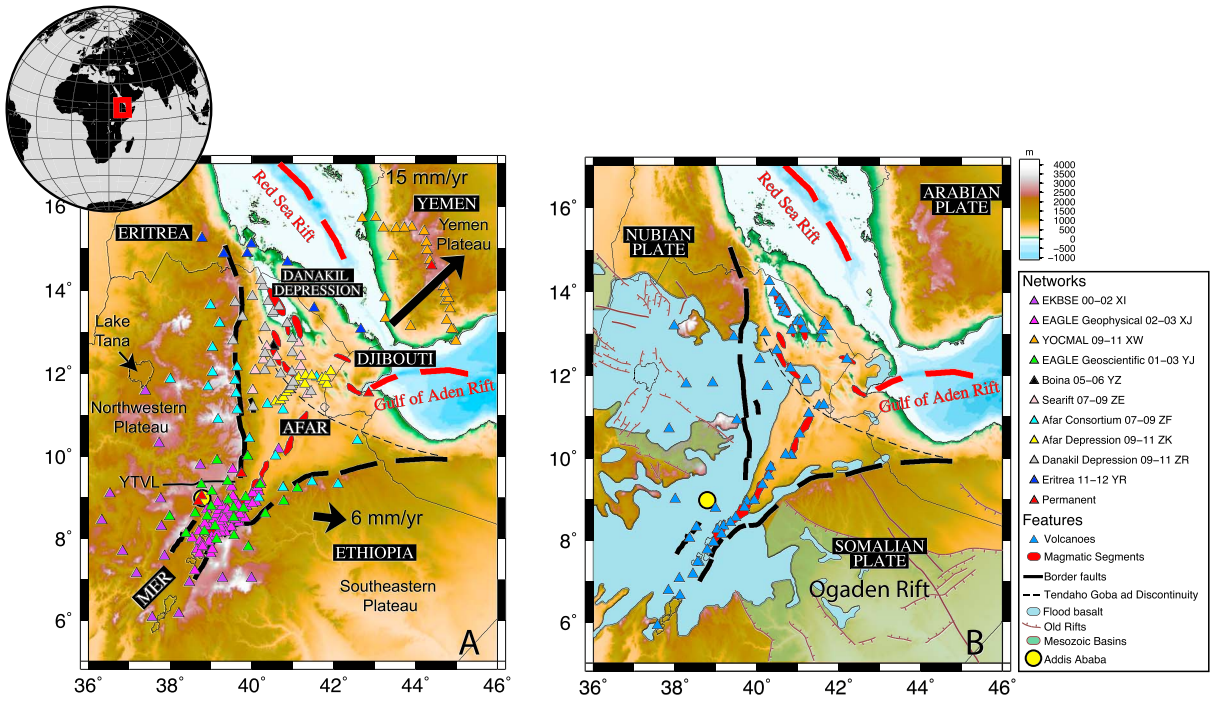

Figure 1. (a) Seismic Station map of the northern East African Rift. Thick black lines show border faults, red polygons magmatic segments, and dashed lines the Tendaho-Goba'ad discontinuity (TGD). Stations are triangles colored to their project deployment with pink (EAGLE 02–03), light pink (Searift), yellow (Afar Depression), gray (Danakil Depression), and black (Boina) networks not used for ambient noise prior to this study. Addis Ababa is marked by a yellow circle. (b) Geological map. Volcanoes are represented by blue triangles and magmatic segments red polygons. Flood basalt provinces are shown in blue and rifts are bordered by brown faults and filled in green.

from continental rifting to oceanic spreading (Makris & Ginzburg, 1987). The EAR forms one arm of the Afar triple junction while the other two arms, the Red Sea and Gulf of Aden rifts, have progressed to full seafloor spreading (Bonatti, 1985; McKenzie et al., 1970).

In this paper we use ambient noise tomography (ANT) from Rayleigh waves (Bensen et al., 2007; Shapiro et al., 2005; Shapiro & Campillo, 2004) to image the uppermost mantle and crustal structure in the northern EAR. Previous studies have used a variety of methods to analyze the crustal structure within rift segments including applying ANT to the MER and Afar, two sections of our study region. One study in Afar produced phase velocity maps and not inverting for shear velocity (Korostelev et al., 2015), while a second study focused on the northern and central sections of the MER using group velocities before inverting for absolute shear velocity (Kim et al., 2012). These studies found slow velocities at all depths beneath the rift flanks suggesting protracted magmatic modification of the crust coupled with two magmatic zones beneath the MER, indicative of a complex magmatic plumbing system (Kim et al., 2012; Korostelev et al., 2015). However, to facilitate direct comparisons between regions and thereby interpret evolution of rifting processes in space and time, we require a complete and self-consistent model for the northern EAR. Here we utilize five additional seismic networks (Figure 1a) and produce a crustal model for areas of Ethiopia, Eritrea, Djibouti, and the southwest of Yemen, allowing direct comparison of regions at different stages of rifting. The absolute shear wave velocity model is used to interpret crustal structure and how rifting modifies the lithosphere by tectonic and magmatic processes. Shear wave velocities also allow us to infer areas containing fluids which will aid us in constraining where fluids, and potentially melt, reside within the crust and mantle.

2. Geological Background

Ethiopia is underlain by Precambrian basement formed during the Neoproterozoic Pan-African orogeny (Mège & Korme, 2004; Figure 1b). The basement is composed of magmatic, metamorphic, and sedimentary rocks (Berhe, 1990; Braathen et al., 2001; Kazmin et al., 1978; Merla et al., 1973), which have been crosscut

by northwest-southeast trending Precambrian fractures (Mège & Korme, 2004). During the late Paleozoic to Mesozoic these fractures were reactivated to form several failed rift basins (Corti, 2009; Ebinger et al., 2000; Mège & Korme, 2004).

Volcanism initiated 45 Ma beneath our study area and continues to recent times (e.g., Barnie et al., 2016; Rooney et al., 2014; Siegburg et al., 2018). The largest event was the emplacement of the ~2-km-thick flood basalt sequence 31–29 Ma (Hofmann et al., 1997; Ukstins et al., 2002), covering an area ~600,000 km^2 (Rooney, 2017; White & Mckenzie, 1989). The flood basalts were later interspersed with shield volcanoes 22–11 Ma (e.g., Mount Choke, Guna, and Guguftu; Beccaluva et al., 2009; Kieffer et al., 2004). Present-day volcanic activity is largely focused in the ~70-km long and 20-km wide en echelon magmatic segments within the rift axis (Barnie et al., 2016; Ebinger & Casey, 2001; Hayward & Ebinger, 1996; Rooney et al., 2014; Siegburg et al., 2018; Wolfenden et al., 2004). Recent volcanism also occurs off-axis such as in the Yerer-Tullu Wellel Volcanotectonic Lineament (YTVL) and around Lake Tana (Keranen & Klemperer, 2008; Kieffer et al., 2004; Figure 1).

Approximately coeval with the main flood basalt emplacement 31–29 Ma was the onset of rifting (Bosworth et al., 2005; Wolfenden et al., 2004), subsequently forming the Red Sea and Gulf of Aden Rifts (Hofmann et al., 1997; Pik et al., 1998). Rifting initiated later at 20 Ma in the Southern MER, and 18–11 Ma for the central and northern sections (Kazmin et al., 1978; Wolfenden et al., 2004). The three rifts form the Afar triple junction separating the Nubian Somalian and Arabian plates (Figure 1b; Ebinger et al., 1993; McKenzie et al., 1970; Wolfenden et al., 2004). On a smaller scale, Oligocene-Miocene border faults separate the plateaus (northwestern and southeastern) from the rift in the MER and Afar (Figure 1a; Corti et al., 2013). Within Afar, the locus of extension shifted from the border faults to smaller faults and volcanic segments at around 10 Ma (Wolfenden et al., 2005). In southernmost Afar and the MER, extension localized to the rift axis later at 6.6–3 Ma (Wolfenden et al., 2004). Geodetic constraints in the MER and Afar suggest that >80% of the present-day extension is focused within the magmatic segments (Bilham et al., 1999; Ebinger & Casey, 2001). The rifting rates vary between regions with full spreading rates of 18, 16, and 6 mm/year for the Red Sea Rift (McClusky et al., 2010; Vigny et al., 2006), Gulf of Aden Rift (Jestin et al., 1994; Vigny et al., 2006), and MER, respectively (Casey et al., 2006; Jestin et al., 1994; Saria et al., 2014; Figure 1b).

Rifting processes have modified the crust resulting in variations in crustal thicknesses throughout the region. The thickest crust is found beneath the plateaus with the southeastern plateau 35- to 40-km thick and the northwestern plateau 40- to 45-km thick (Hautot et al., 2006; Mackenzie et al., 2005; Stuart et al., 2006). The crust thins into the MER where the crust is 38-km thick in the south and 30 km beneath the northern MER (Hammond et al., 2011; Maguire et al., 2006; Stuart et al., 2006). In Afar, the crust is ~26-km thick, thinning to ~16 km beneath the Danakil depression, the thinnest crust in the region (Dugda et al., 2005; Dugda & Nyblade, 2006; Hammond et al., 2011; Lavayssiere et al., 2018).

The mantle beneath the region is thought to have elevated temperatures and pervasive melt based on seismic, geochemical, and geodynamic studies (Armitage et al., 2015; Bastow et al., 2005; Ferguson et al., 2013; Gallacher et al., 2016; Lavayssiere et al., 2018; Rooney et al., 2012; Rychert et al., 2012). Mantle seismic velocities are slower than the global average (Bastow et al., 2005, 2008; Fishwick, 2010; Gallacher et al., 2016; Stork et al., 2013), which complements geochemical and geodynamic studies of inferred elevated mantle temperatures of 100–170 °C above normal mantle temperatures (Armitage et al., 2015; Rooney et al., 2012). Beneath the rift, velocities are typically slow with an absence or low-amplitude lithosphere-asthenosphere boundary (Lavayssiere et al., 2018; Rychert et al., 2012), interpreted by some previous studies as evidence of decompression melting or dyke-induced lithospheric thinning (Havlin et al., 2013; Rychert et al., 2012; Stork et al., 2013). The MER axis also displays slow mantle velocities, which have previously been interpreted as evidence for partial melt generated by ongoing rifting processes (Bastow et al., 2005; Gallacher et al., 2016; Hammond et al., 2013).

3. Methods

We use data from continuous vertical component seismometers recorded by 10 temporary and 4 permanent networks (Figure 1a) between 1999 and 2012. The vertical component data from each of the 170 stations was split into 24-hr sections and resampled to 1 Hz. Instrument responses were removed and the waveforms were then normalized and whitened with a bandpass filter of 0.005–0.14 Hz (Bensen et al., 2007). Cross

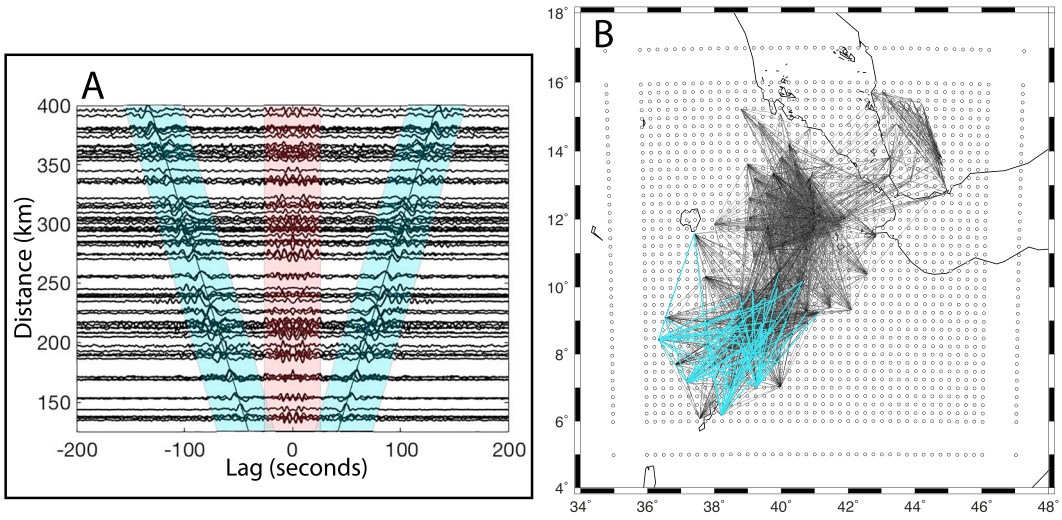

Figure 2. (a) Example noise correlation functions plotted as a function of distance and lag. Rayleigh waves highlighted in light blue with *P* wave arrivals (unused) in red. (b) Nodal grid at 0.25° spacing overlain with ray paths at 18 s in black. Blue lines are ray paths used in Figure 2a.

correlations and linear stacking were performed between all pairs of concurrently running stations with >10 days of continuous recording, using the methods of Bensen et al. (2007), Harmon et al. (2007, 2008), and Harmon and Rychert (2016), resulting in 4,820 noise correlation functions (NCF; Figure 2a).

We estimate the phase velocities from the NCF in the following way. We first estimate the average phase velocity dispersion across the region using a spatial domain technique using the entire array. We accomplish this by fitting a zeroth-order Bessel function of the first kind as a function of interstation distance, frequency, and phase velocity, to the real part of the fast Fourier transformed NCF by searching over phase velocities from 2.5–5 km/s in a 0.01-km/s step at each period of interest (Harmon et al., 2008, 2010). Then for each individual NCF the phase was measured at each period of interest by unwrapping the phase of the stacked NCF using the average phase velocity curve at the longest periods to resolve cycle ambiguity (Bensen et al., 2007; Harmon et al., 2008). We then used the phase delay from the phase estimates to calculate the phase velocity as the distance between the two stations divided by the phase delay time (Harmon et al., 2007).

We use a two-stage inversion to generate our 3-D shear velocity model. We first invert the measured phase for phase velocity maps using the method of Harmon et al. (2013) from 8- to 33-s period. We parameterize our model space for phase velocity using a 0.25° × 0.25° nodal grid (Figure 2b) and use the average phase velocity at each period as the starting model. The phase velocity inversion uses 2-D finite frequency kernels (Nishida, 2011; Tromp et al., 2010) and an iterative damped least squares approach (Tarantola & Valette, 1982). The sensitivity kernels for each NCF are averaged onto each node. We assign a nominal a priori standard error for each node of 0.2 km/s and fix the Vp/Vs ratio to 1.8, based on averaged receiver function results (Hammond et al., 2011; Stuart et al., 2006). For a given period, we only invert phase data for NCFs with interstation distances greater than twice the wavelength and apply a smoothing factor of 40 km. In the second stage, we invert the phase velocity maps across all periods at each point in the map to generate a 3-D velocity structure, using the best fit shear velocity model from the 1-D dispersion curve as our starting model. For the shear velocity inversion, we use a damped least squares approach (Tarantola & Valette, 1982) and parameterize the shear velocity at every 5 km vertically with 0.1° × 0.1° pixel size. We calculate the partial derivatives that relate variations in shear velocity to changes in phase velocity using DISPER80 (Saito, 1988). Although our shear velocity models are discretized at 5-km intervals in depth, we interpolate the velocity structure in depth to 1-km depth for presentation purposes using a linear interpolation.

Across the study region there are variations in sediment thickness and large bodies of water which may bias shear velocity structure to slower velocities at depth if not properly accounted for. We tested the effects of large slow layers on our shear velocity model by imposing a water layer to a thickness of 3 and 5 km in the Red Sea and Gulf of Aden with velocity and density values a priori from CRUST1.0 (Laske et al., 2013). We

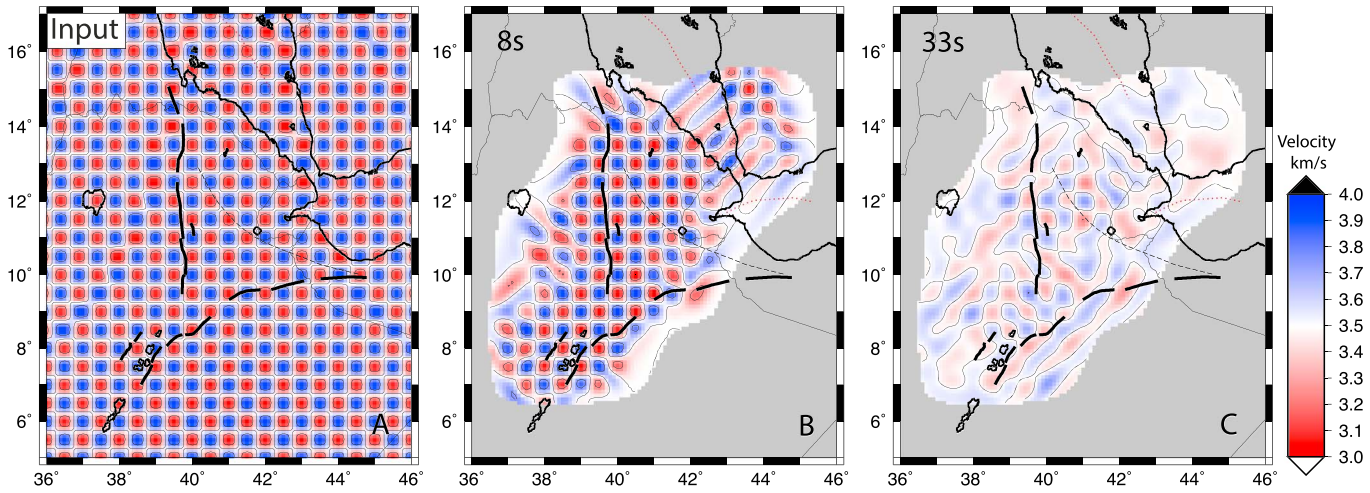

Figure 3. Checkerboard tests for 0.5° × 0.5°. Initial model shown in (a) with (b) and (c) showing the resultant output model at 8 and 33 s, the limits of our study. Results are cropped outside the 0.7 standard error contour. See text for details.

also performed the same tests with a sediment layer in the rifts using sediment thickness from CRUST1.0 (Laske et al., 2013). After nine iterations, these tests produced shear velocity models that were within error of our preferred model, leading to confidence in our results.

4. Resolution and Errors

We assess the minimum interpretable length scales of our velocity anomalies by presenting checkerboard tests for 0.5° × 0.5° anomalies between 8- and 33-s period. The tests indicate we can resolve anomalies at the scale of 0.5° across most of the region (Figure 3), particularly in regions with good ray path coverage within the MER and northwestern Afar (Figure 2b). In areas of sparser ray coverage such as eastern Afar, the Red Sea, and Gulf of Aden we have poorer resolution and northeast-southwest smearing of checkerboard tests. Consequently, we do not interpret these regions. We mask results outside the standard error contour of 0.07 km/s, the approximate contour of the 2σ error, from the linearized phase velocity inversion.

We assess the vertical resolution of the shear velocity via the formal resolution matrix of the shear velocity inversion. Our model is not well resolved above 5 km and below 60-km depth with formal resolution values <0.10. Formal resolution values are typically around 0.37 for each 5-km thick layer in the 10- to 55-km depth range indicating we have independent constraints approximately every 10–15 km in depth. In other words, we can resolve average velocity variations over 10- to 15-km depth ranges.

5. Results

5.1. Phase Velocities

Our average 1-D phase velocity dispersion curve for the full study region ranges from 3.13 ± 0.03 km/s at 8-s period to 3.61 ± 0.05 km/s at 33-s period (Figure 4a). From our final velocity maps (Figures 5 and 6), we take 1-D phase velocity curves from individual pixels in the maps and their corresponding 1-D shear velocity profiles (Figure 7), allowing us to directly compare regions of interest labeled from “a–h.” The slowest phase velocities for all depths are located within the MER (Figures 7a and 7b, “a,” “g,” and “h”) ranging from 3.18 ± 0.03 km/s at 8-s period to 3.56 ± 0.05 km/s at 33-s period. The Danakil depression, “c,” has the fastest velocities from 3.21 ± 0.04 km/s at 8-s period to 3.60 ± 0.06 km/s at 33-s period. At short periods of 8 to 13 s we observe slow velocities at “e” beneath the northwestern plateau. In general, the plateau regions, “d–f,” have faster phase velocities at shorter periods than the MER and Afar averages, “a–c.”

Within our phase velocity maps (Figure 5), we observe variations across the region that correlate with surface geologic and tectonic features. For example, we observe slow velocities beneath the MER at all periods, with minimum velocities ranging from 2.95 ± 0.03 km/s at 8-s period, to 3.45 ± 0.05 km/s at 33-s period (Figures 5a–5d “a”). Beneath Afar we observe moderate velocities with maximum velocities ranging from

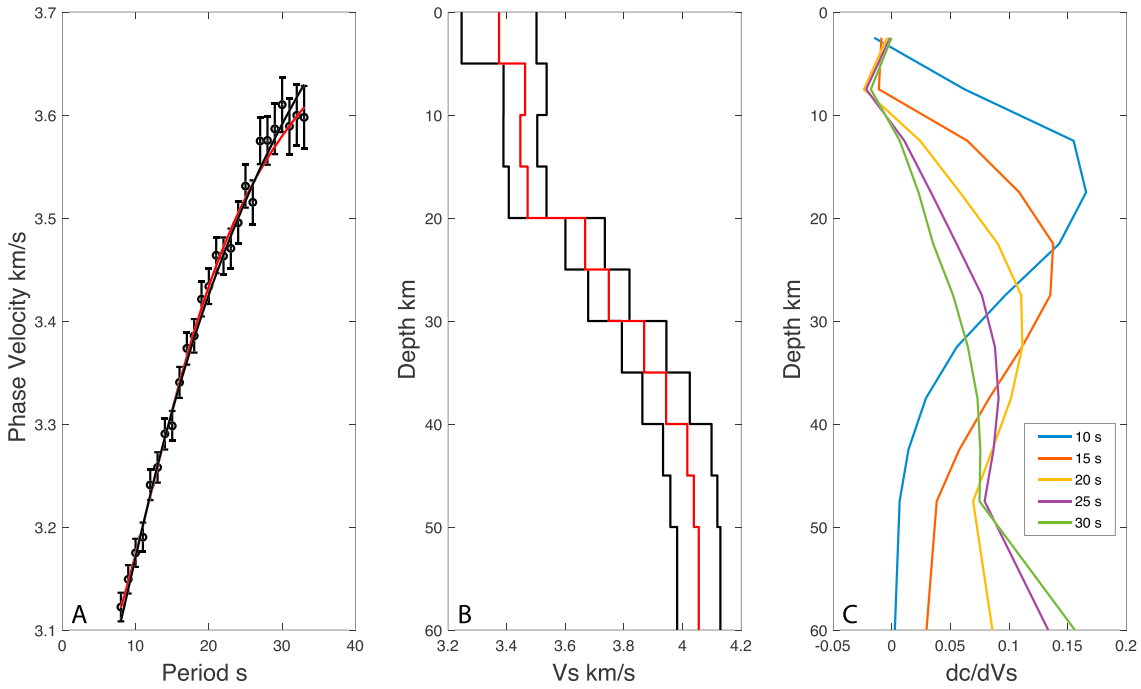

Figure 4. (a) Average 1-D phase velocity for the study region with 3σ error bars (circles) with predicted dispersion from Gallacher et al. (2016, black line) and our best fit shear velocity model dispersion overlain (red line). (b) Best fit shear velocity model for the study region (red line) and formal 2σ error bounds (black lines). (c) Sensitivity kernels for Rayleigh waves at selected periods.

3.30 ± 0.04 km/s at 8-s period to 3.65 ± 0.06 km/s at 33-s period (Figures 5a–5d "b–c"). The northwestern plateau has the greatest lateral velocity variations, with minimum velocities ranging from 3.00 ± 0.05 km/s at 8-s period, to 3.55 ± 0.07 km/s at 33-s period (Figures 5a–5d "d") and maximum velocities ranging from 3.35 ± 0.05 km/s at 8-s period, to 3.70 ± 0.07 km/s at 33-s period at "f". In contrast, phase velocities for the southeastern plateau are more laterally homogenous, with phase velocities of 3.30 ± 0.05 km/s at 8-s period increasing to 3.60 ± 0.07 km/s at 33-s period (Figures 5a–5d "e"). Although at 8-s period, the phase velocity map exhibits the greatest lateral heterogeneity.

5.2. Shear Velocities

Our average 1-D shear velocity model across all nodes ranges from 3.36 ± 0.04 km/s at 5-km depth to 4.04 ± 0.05 km/s at 60-km depth (Figure 4b). Our best fit model does not have a fast lid or slow velocity zone visible at mantle depths, rather shear velocity monotonically increases with depth. One-dimensional profiles through our shear velocity volumes (Figure 7c snd 7d) show similarities to the phase velocity maps. The slowest velocities for all depths are again located within the MER, "a," ranging from 3.28 ± 0.03 km/s at 10-km depth to 3.83 ± 0.04 km/s at 40-km depth, with a broad velocity increase from 20- to 50-km depth. Within Afar, "b," velocities increase from 3.45 ± 0.04 km/s at 10 km and increase to 3.86 ± 0.05 km/s at 40-km depth, with the sharpest gradient between 5- and 20-km depth. The Danakil depression, "c," has the fastest velocities from 3.64 ± 0.04 km/s at 10-km depth to 3.98 ± 0.06 km/s at 40-km depth, again with the sharpest gradient between 5- and 20-km depth. The Danakil depression, in contrast to the starting model and most of our study region, requires a fast lid, with a slow velocity zone minimum at 45-km depth. Beneath the northwestern and southeastern plateaus, "e and f," we observe fast shear velocities of 3.5 ± 0.05 km/s to 3.85 ± 0.07 km/s at 40-km depth. The exception to this is the slow-velocity zone beneath "d," where velocities are slower at 3.3 ± 0.05 km/s at 10-km depth. Velocities become progressively faster until 40-km depth where they are similar to the overall plateau velocity structure.

Absolute shear wave velocity maps (Figure 6) show similarities to phase velocities, ranging from 3.20–4.10 ± 0.06 km/s. At 40–60 km, mantle depths, we observe velocities ranging from 3.60–4.10 ± 0.06 km/s beneath the region. These are all slower than the global model ak135 which has a velocity of 4.48 km/s

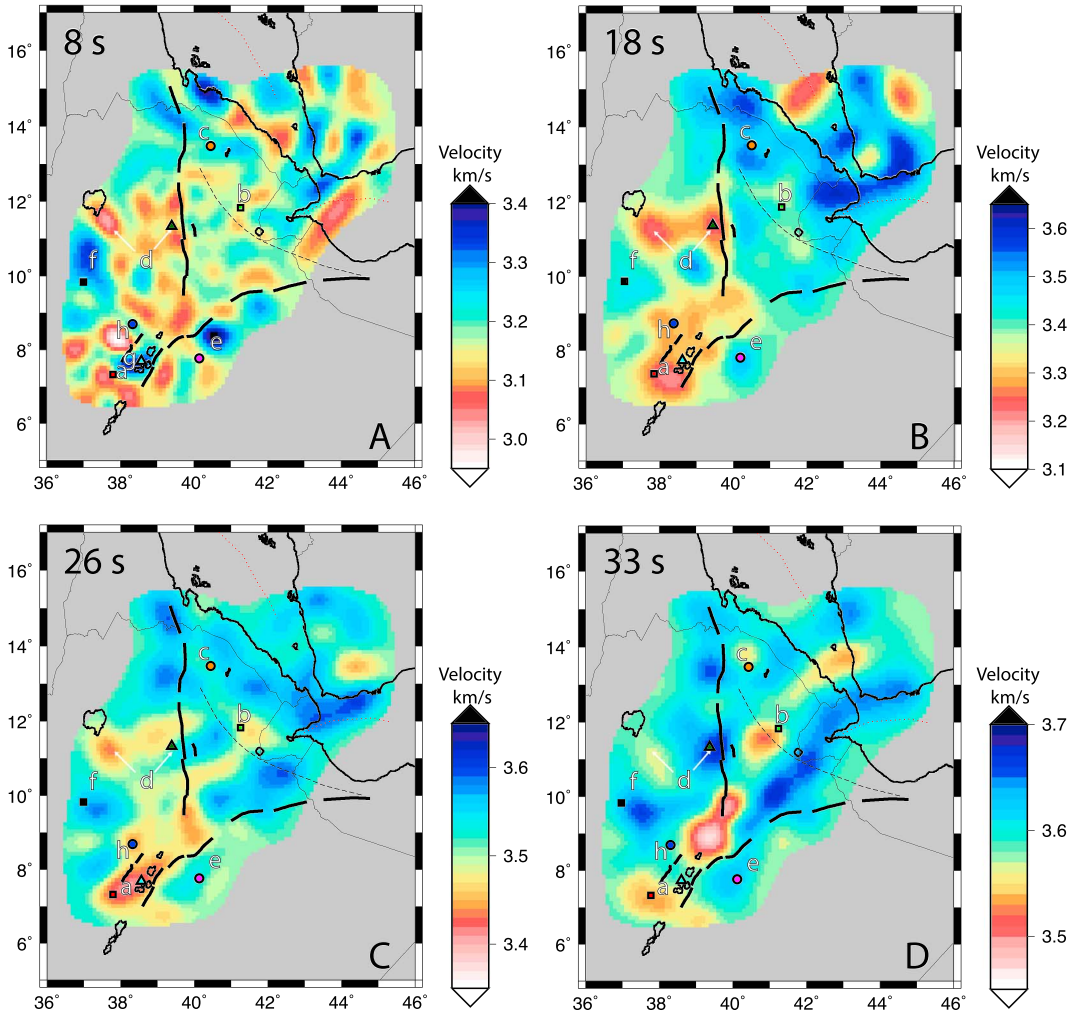

Figure 5. (a–d) Phase velocity maps resulting from tomographic inversion of ambient noise dispersion data at 8, 18, 26, and 33 s respectively. Models have been cropped to the standard error contour. Red indicates slower velocities and blue faster velocities. Sections get, on average, progressively faster with depth. Colored symbols indicate the locations of profiles shown in Figure 7. Thick black lines indicate border faults. Letters a–h are regions referred to in the text.

for mantle beneath the continents (Kennett et al., 1995). We observe slow velocities beneath the MER at all depths, with minimum velocities ranging from 3.20 ± 0.03 km/s at 10-km depth to 3.75 ± 0.04 km/s at 40-km depth (Figure 6 "a"). The slow velocity anomaly is roughly 200-km long by 100-km wide trending along the rift valley. It is broad and distributed at depth, becoming focused to the rift valley in the crust. A smaller slow velocity region follows the surface trend of the YTVL (Figures 6a–6c "h"). The anomaly is approximately 50-km wide trending east–west with velocities of 3.20 ± 0.03 km/s at 10-km depth increase to 3.60 ± 0.04 km/s at 30-km depth. While most of the MER displays slow velocities, at "g" we observe a zone of faster velocity, relative to the surroundings, between the Aluto and Corbetti volcanoes with velocities of 3.65 ± 0.03 km/s above 20-km depth, approximately 40 km in diameter (Figures 6a, 6b, and 8a).

Beneath Afar, velocities are fast everywhere relative to the MER, with maximum velocities ranging from 3.75 ± 0.04 km/s at 10-km depth to 4.05 ± 0.06 km/s at 40-km depth (Figures 6a–6d "b and c"). Beneath most of the active magmatic segments (Figure 6, open red polygons and "b") in Afar, we observe slower velocities down to 3.45 ± 0.04 km/s at 10-km depth and 3.85 ± 0.06 km/s at 40-km depth. The transition from the MER into Afar is also marked by a distinct 5% increase in velocity where the rift widens into Afar.

While the MER and Afar are broadly consistent within their regions, the plateaus display greater heterogeneity, with lateral variability of 0.5 km/s as compared to 0.3 km/s outside the plateaus. The velocities

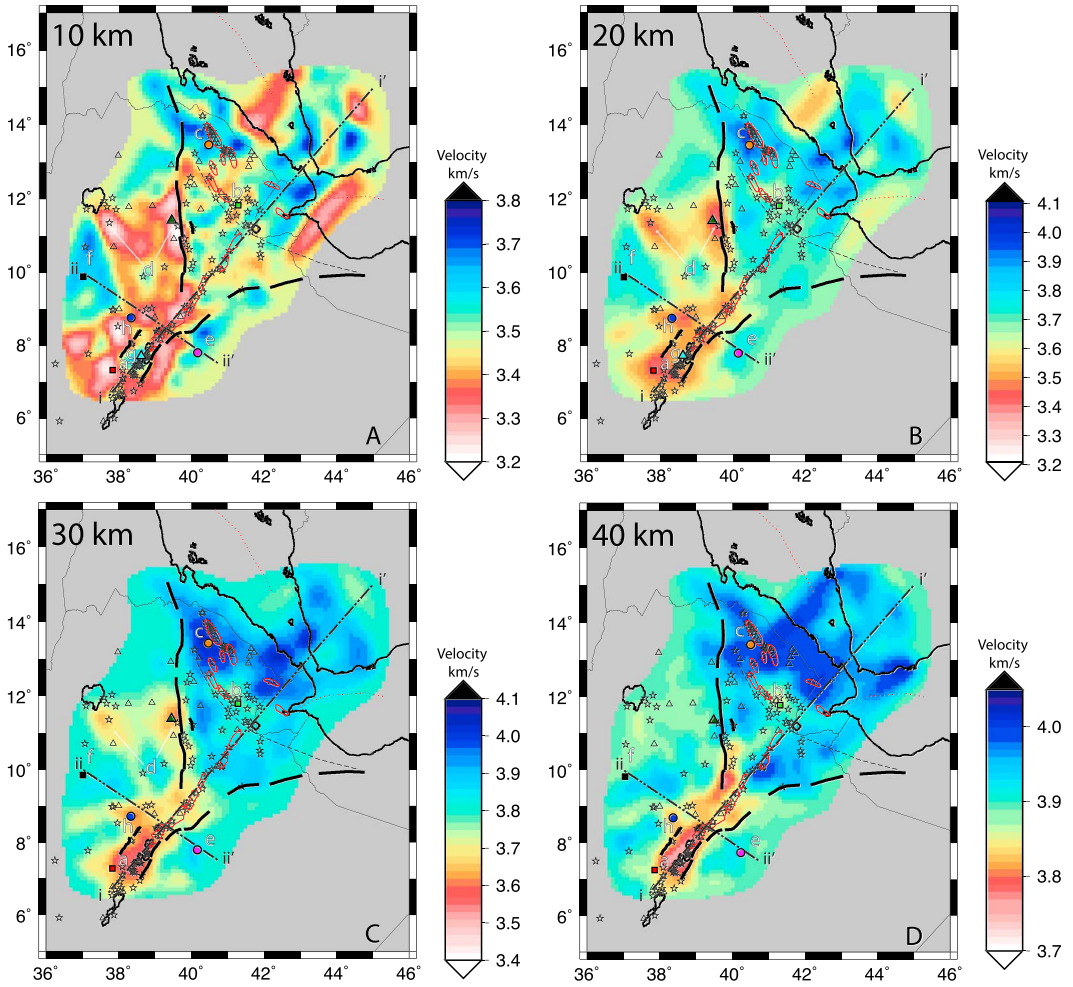

Figure 6. (a–d) Interpolated depth slices at 10, 20, 30, and 40 km, respectively. Sections get progressively faster with depth with the vertical resolution smoothed across 10 km. Dashed black lines show cross sections in Figures 8a and 8b with thick black lines indicating the border faults. Letters a– h are regions referred to in the text. One-dimensional profile locations (colored symbols) are described in Figure 7. Red polygons indicate magmatic segments, black triangles volcanoes, and black stars geothermal activity.

beneath the majority of the plateaus are fast, typically around 3.65 ± 0.05 km/s at 10-km depth and ~3.95 ± 0.07 km/s at 40-km depth (Figures 6 and 7 "e–f"). However, in localized regions, velocities are in some cases as slow as the MER. For example, near "d" on the northwestern plateau (Figures 6a–6c and 8b), velocities are as slow as 3.25 ± 0.05 km/s at 10-km increasing to 3.65 ± 0.07 km/s at 30-km depth. In addition, on the Yemen Plateau the velocity is 3.30 ± 0.05 km/s at 10 km, and this slow velocity continues down to 20-km depth (Figures 6a, 6b, and 8a).

5.3. The Lower Crust and Moho

Based on the studies of Keranen et al. (2009) the Moho beneath the MER can be approximated with an absolute shear velocity of 3.75 km/s. We produce two transects through our model, along the rift and across the MER, approximately coinciding with the EAGLE active source line (Figure 8) and use this 3.75 km/s contour as a proxy for Moho depth. We then compare to previous direct measures of crustal thickness from receiver function studies (Dugda et al., 2005; Hammond et al., 2011; Stuart et al., 2006). To do this we interpolate the model to every 1 km and take a velocity slice at 3.75 km/s and overlay crustal thickness from receiver function studies in Afar (Hammond et al., 2011), and the MER (Figure 9; Dugda et al., 2005; Stuart et al., 2006). Along the rift we see the 3.75-km/s contour shallowing from 40 km beneath the MER to 20 km in Afar. The crust is relatively thin beneath the Red Sea (17 km) and thickens to 29 km beneath Yemen (Figure 8a). There is some agreement between the 3.75-km/s contour and crustal thickness studies in the MER and Afar rifts;

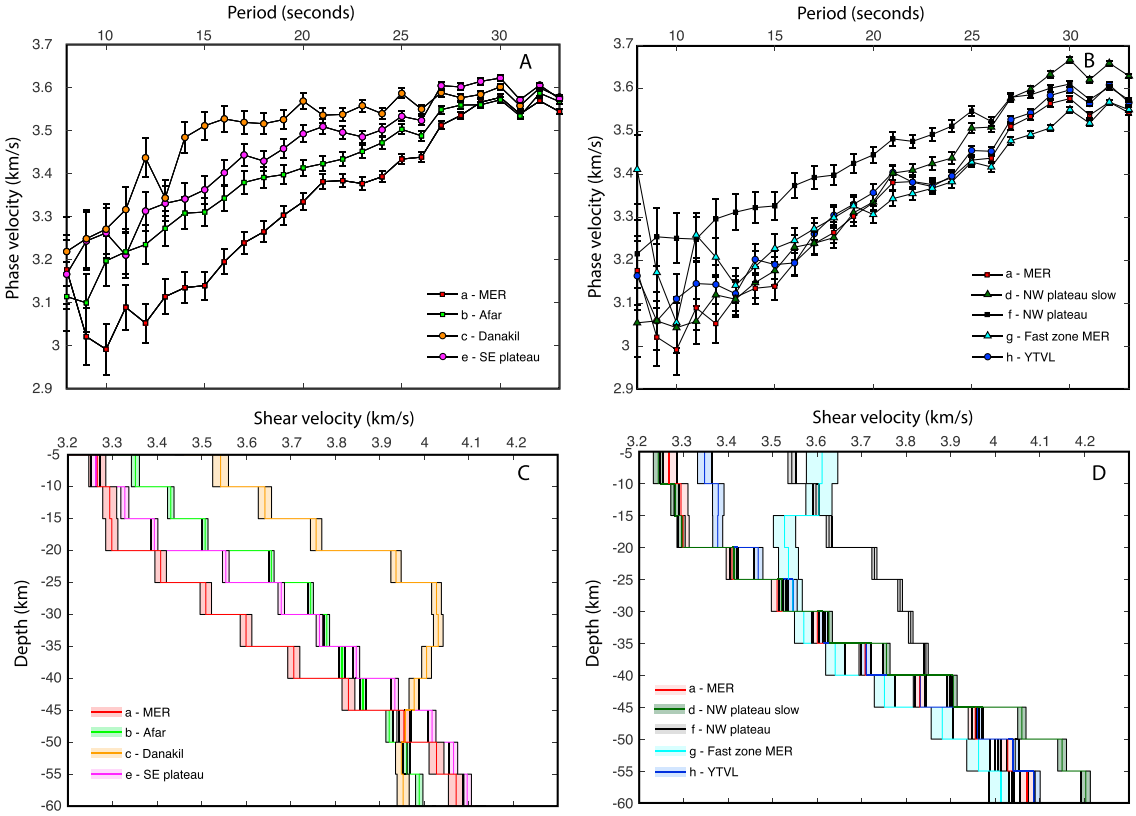

Figure 7. One-dimensional phase and shear velocity profiles for key areas discussed in the text. (a) Phase velocities comparing the MER, Danakil, Afar, and southeastern plateau. Error bars are 3σ error. (b) One-dimensional profiles for the plateau and MER regions. Panels (c) and (d) are same as (a) and (b) but for shear velocities. See Figures 5 and 6 for 1-D profile locations. MER = Main Ethiopian Rift.

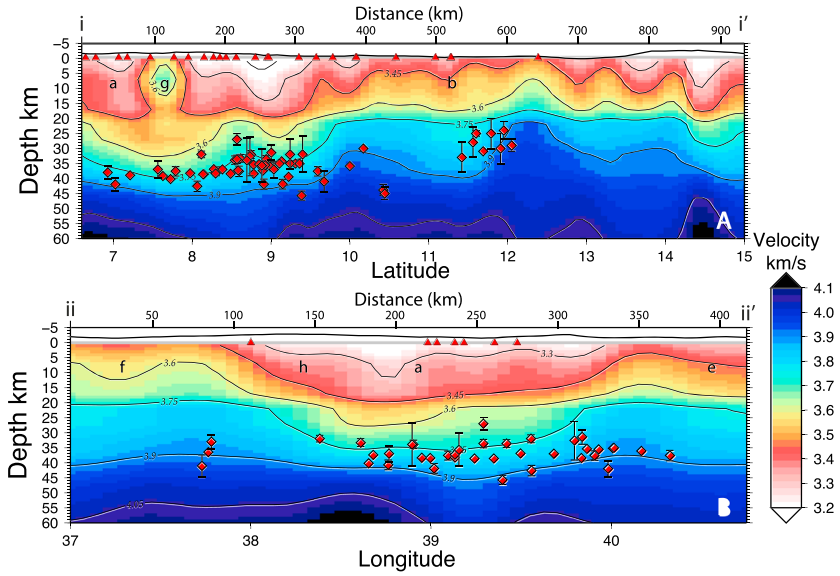

Figure 8. Cross sections of the shear velocity maps, interpolated to 1-km depth resolution. See Figure 6 for locations of cross sections. (a) Profile along the rift axis. (b) Profile across the MER and plateau. Receiver function Moho depths plotted as diamonds within 1° of the profile (Ayele et al., 2004; Dugda et al., 2005; Hammond et al., 2011; Stuart et al., 2006).

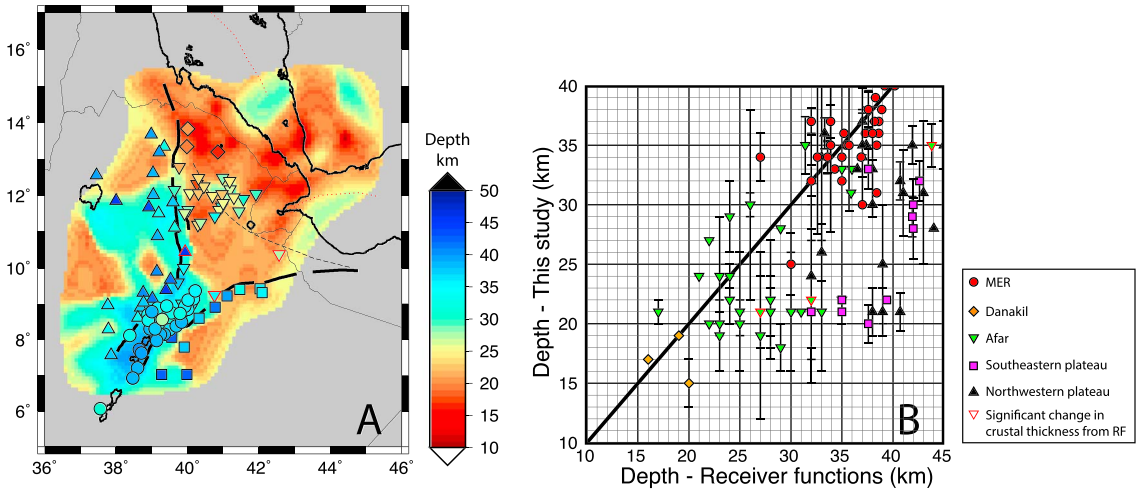

Figure 9. (a) Interpolated velocity slice at 3.75 km/s used as an indicator for crustal thickness. Symbols are depths from receiver function studies (RF) for regions within Ethiopia (Ayele et al., 2004; Dugda et al., 2005; Hammond et al., 2011; Stuart et al., 2006). (b) Depth to the Moho from receiver function studies versus this study. Colors and symbols represent different regions. Please see the legend for details. MER = Main Ethiopian Rift.

however, many points do not appear to correlate. Across the rift axis (Figures 8b and 9) and beneath the northwestern and southeastern plateaus, we no longer match the estimates of crustal thickness. Here we observe depths of ~20–37 km compared to 32–45 ± 3 km on the northwestern plateau and 20–38 km compared to 32–43 ± 3 km for the southeastern plateau (Figure 9b). There are also some differences between the Moho and 3.75-km/s contour in regions where crustal thickness changes over short distances (e.g., from the plateau into Afar, and near the TGD in Afar). Our model laterally smooths across these short length scales and therefore does not fully recover sharp gradients in crustal thickness and the sharp increase in velocity at the Moho (Figure 9).

6. Discussion

Our velocity model constrains shear wave velocities of the crust and uppermost mantle. The key observations of our shear wave velocity model are: (1) Velocities in the uppermost mantle are everywhere slower than the global average for continents using ak135, in particular beneath the MER (3.75 ± 0.04 km/s); (2) the MER is significantly slower than Afar with a clear increase in velocity at all depths as the rift widens into Afar; and (3) the Ethiopian plateau displays heterogeneity in crustal velocity. In the following section, we use our velocity maps to interpret velocity variations and use these to answer key questions about the nature of the crust and mantle structure when rifting modifies the lithosphere during the rifting to breakup process. This will allow us to identify where fluids, and potentially melt, reside within the crust and mantle.

6.1. Mantle Velocities

Mantle velocities in our region are anomalously slow, when compared to global averages appropriate for continental regions such as iasp91, by up to 9–16% over the uppermost mantle. Previous studies in the region have found similarly slow velocities in the mantle, for example, Gallacher et al. (2016) and Keranen et al. (2009) found values of 3.8–4.0 km/s and 3.9–4.2 km/s, respectively. The low values are also similar to slow shear velocities observed in mid ocean ridge systems such as the southern East Pacific Rise (~3.9 km/s; Harmon et al., 2009), the Eastern Lau Back Arc Spreading Center (~3.6 km/s, Wei et al., 2015), and the Juan De Fuca/Gorda Ridges (~3.8 km/s Gao, 2016). Although there are significant differences in the tectonic environments the possible causes for these anomalously slow velocities are likely similar, mantle upwelling, and associated volcanism at the surface.

6.1.1. Possible Causes for Anomalously Slow Mantle Velocities

In this region shear velocities are everywhere slower than expected for a mantle peridotite composition (<4.1 ± 0.06 km/s including beneath the plateau) in the uppermost mantle down to 60-km depth (Hacker & Abers, 2004). Compositional variation in peridotites yields little shear velocity reduction (<1.5%) for the range of expected densities and compositions (Lee, 2003; Schutt & Lesher, 2006). Mantle composition in

the northern EAR has heterogeneity but is predominantly peridotite (Rooney et al., 2017). We therefore do not think that variation in composition across the region is the cause of the slow velocities we observe.

In the upper mantle, shear velocities are sensitive to variations in temperature and grain size (Faul & Jackson, 2005; Jackson & Faul, 2010). Mantle velocities of 3.60–4.10 km/s, a 9–16% reduction from the global average, are likely accommodated at least in part by an increase in mantle temperature and/or grain size changes. Petrological estimates and models suggest a mantle potential temperature for this region of between 1350 °C (Armitage et al., 2015; Pinzuti et al., 2013; Rychert et al., 2012) and 1490 °C (Armitage et al., 2015; Ferguson et al., 2013; Rooney et al., 2012) and therefore ranging from normal ambient mantle to ~140 °C hotter than average (Rooney et al., 2012). We use a Burgers model relating shear velocity and temperature (Jackson & Faul, 2010), for a peridotite mantle at grain sizes between 1–20 mm, (based on xenoliths in the MER; Rooney et al., 2005) with an estimate for the geotherm for the MER, to determine the mantle temperature required to match our observations. We require a temperature between 1650 °C and 1900 °C for grain sizes of 1–20 mm, respectively. This temperature is 160–550 °C hotter than predicted estimates, requiring additional explanations for the slow mantle velocities. At a given temperature grain size changes can also reduce velocity by up to 3% (Faul & Jackson, 2005; Jackson & Faul, 2010) when grain size is increased from 1–20 mm. However, grain size cannot in and of itself explain our observations again requiring an additional explanation.

We therefore require a fluid component, most likely partial melt, at greater depths and potentially hydrothermal fluids shallower. Assuming slower velocities in the upper mantle are from melt we can use the relationship of 1% melt slows shear velocities by 7.9% (Hammond & Humphreys, 2000). We find 1.1% melt beneath both plateaus and 2.0% melt beneath the slowest region of the MER. These values are similar to previous teleseismic tomography studies where partial melt of 0.6–4% are calculated (Bastow et al., 2011; Civiero et al., 2015, 2016; Ferguson et al., 2013; Gallacher et al., 2016). Forward modeling of the crust and mantle found similar values of <5% melt (Armitage et al., 2018). Variations in melt percentage within the mantle to previous tomography studies may arise from greater ray path density and broader frequency content, particularly the inclusion of high frequencies, compared to teleseismic techniques (Shapiro et al., 2005; Shapiro & Campillo, 2004). *Vs* studies will have more significant velocity reductions, relative to *Vp*, in the presence of melt (Karato, 2004).

We also observe slow mantle velocities, compared to global average velocities, at Moho depths (defined by receiver functions; Dugda et al., 2005; Hammond et al., 2011; Stuart et al., 2006). The Moho is an interface which previous modeling studies using magnetotelluric and seismic data propose to be an area of 2–7% melt accumulation (Armitage et al., 2015, 2018; Desissa et al., 2013). We therefore suggest that partial melt is more localized near the Moho than at depth.

6.1.2. The Moho and Lower Crustal Intrusions

Inferred crustal thickness beneath our study region using a 3.75 km/s contour, are broadly consistent with previous direct measures of crustal thickness particularly beneath the MER and Afar from receiver functions and active source studies (Ayele et al., 2004; Dugda et al., 2005; Hammond et al., 2011; Maguire et al., 2006; Stuart et al., 2006; Figure 9). Within the rift, the 3.75-km/s contour shallows from the MER to Afar which is likely an effect of crustal thinning with progressive rifting (Hammond et al., 2014; Tiberi et al., 2005). The shallowest inferred Moho depths are beneath the Red Sea and the Danakil depression, in good agreement with receiver function studies (Hammond et al., 2011). Beneath the plateaus the 3.75-km/s contour is shallower than the receiver function-derived Moho depth, implying faster velocities within the lower crust. Faster velocities in the lower crust suggest that the crustal composition has been modified, and we propose that the most likely change is from solidified lower crustal mafic intrusions. Solidified mafic intrusions in the lower crust increase velocity, thereby shallowing the depth of the 3.75-km/s contour and reducing the contrast between lower crustal and mantle seismic velocities (Hammond et al., 2011; Lavayssiere et al., 2018; Stuart et al., 2006; Thybo & Nielsen, 2009). The EAGLE active source experiment also observed a fast velocity *Vp* layer in the lower crust coupled with a dense lower crust beneath the northwestern plateau (Cornwell et al., 2006; Mackenzie et al., 2005; Maguire et al., 2006), while receiver functions observe a reverberation from the top and base of the underplate (Lavayssiere et al., 2018; Stuart et al., 2006). Our crustal thickness estimate based on the 3.75-km/s depth contour would probably select the top of the underplate, yielding apparent thinner crust, thus supporting widespread solidified lower crustal intrusions beneath the plateau.

In contrast to the fast velocities on most of the plateau, we observe a smaller slow velocity region that trends east–west following the surface trend of the YTVL (Figures 6a–6c "h") a line of Quaternary-Recent volcanoes. This suggests we are imaging a thermal or fluid anomaly associated with ongoing magmatic processes. Beneath the eastern end of the YTVL, highly localized high conductivities are seen in magnetotelluric surveys (Whaler & Hautot, 2006) coupled with collocated clusters of lower crustal seismicity (Keir et al., 2009) suggest ongoing, but localized lower crustal melt emplacement within the solidified crust.

6.2. Crustal Velocities

6.2.1. MER Axis

We define crustal velocities for our discussion here using the crustal thicknesses estimated by receiver functions across the region (Ayele et al., 2004; Dugda et al., 2005; Hammond et al., 2011; Stuart et al., 2006). The shear wave velocities range from 3.20 ± 0.03 km/s at 10-km depth to 3.55 ± 0.04 km/s at 30-km with a slow velocity anomaly roughly 200-km by 100-km wide positioned beneath the MER axis (Figure 6 "a"). The observation is in apparent contradiction to the elevated *Vp* for the MER crust at 10- to 30-km depth, as determined by first arrival travel time tomography and the EAGLE-controlled source survey (Keranen et al., 2004; Mackenzie et al., 2005; Maguire et al., 2006). These studies interpreted fast *Vp* values as continental crust intruded by now solidified mafic rock. The presence of solidified mafic rock predicts *Vs* that is faster than we observe. The slow *Vs* is also not explained by widespread silicic or intermediate rock type. These typically have *Vs* of 3.64 and 3.78 km/s (Birch, 1960; Simmons, 1964), faster than we observe, but also contrary to the elevated *Vp* from previous studies. We therefore conclude that rock composition does not broadly explain the slow *Vs* in the MER.

Elevated temperatures would also produce slow velocities within the crust. If we assume that the crust within the rift axis is predominantly gabbroic intrusions (Mazzarini et al., 2013; Rooney et al., 2014), crustal temperatures of 600 °C generate velocities >3.81 km/s (Hacker & Abers, 2004), significantly faster than what we observe. Assuming a diorite composition, velocities reach 3.67 km/s under the same conditions. Therefore, temperature cannot solely account for the velocity reductions beneath the MER and we therefore appeal to a fluid component.

The MER is volcanically active, with geodetic evidence for melt input into crustal magma bodies and interaction with hydrothermal reservoirs (Biggs et al., 2011; Hutchison et al., 2016). Fluids may be present in the form of small volumes of partial melt or from the release of volatiles within cooling magmatic systems (Holtzman & Kendall, 2010; Korostelev et al., 2015). If we assume that the velocity reduction in the crust is solely from melt, we can estimate the amount of melt present using the experimental relationship of 0.1 km/s decrease in shear velocity requires 1% melt (Caricchi et al., 2008). We compare to the *Vs* structure of the southeastern plateau, least modified by rifting. We estimate ~3% melt for the MER, within the range of ~0.5–5% from previous seismic studies (Gallacher et al., 2016; Guidarelli et al., 2011; Hammond, 2014). However, models from magnetotelluric and gravity studies yield higher melt fractions of 3–20% (Cornwell et al., 2010; Keranen et al., 2009; Whaler & Hautot, 2006).

Placing constraints on percent melt is complicated by anisotropy and the alignment and shape of melt (Hammond, 2014; Hammond & Kendall, 2016). Rayleigh waves show a velocity reduction for both horizontally and vertically aligned melt with greater sensitivity to horizontal melt in contrast to Love waves which are more sensitive to vertically aligned melt (Hammond & Kendall, 2016). Furthermore, melt stored as horizontal disks requires up to 10% less melt to generate a reduction in Rayleigh wave shear velocity than spherical melt bodies (Hammond & Kendall, 2016). Geochemical, seismic, and magnetotelluric studies provide evidence for a series of stacked sills at the base of the crust (Ferguson et al., 2013; Hammond, 2014; Johnson et al., 2015) and may suggest that our velocity estimates are biased toward higher quantities of melt due to anisotropy. Further work is required to assess the radial and azimuthal anisotropy across the region to understand the degree of bias.

Generally, our slow velocity anomalies within the crust are spatially correlated along-rift with the active volcanic segments (red polygons, Figures 6a–6d), though our velocities are commonly broader, in part due to the wide lateral sensitivity of Rayleigh waves. While we cannot rule out sediment infill to explain slow shear velocities near the surface (Christensen, 1996; Hacker & Abers, 2004; Mazzarini et al., 2013), it is more likely that the velocities are associated with the active magmatism in the rift axis. The slow velocities end at the southern extent of the visible magmatic segments where we observe a fast velocity of 3.65 ± 0.03 km/s

above 20-km depth (Figures 6a, 6b and 8a "g"). Slower velocities are more widespread at depth near the Moho with the slowest velocities being beneath the rift. The slow velocities are present at all depths within the crust beneath the rift axis.

6.2.2. Afar

The Afar crust has relatively fast *Vs* in our study (3.75 ± 0.04 km/s at 10-km depth to 4.05 ± 0.06 km/s at 40-km depth) excluding "b" at 10-km depth where velocities are as slow as 3.45 km/s (Figure 6a). This observation is consistent with fast *Vp* imaged previously (Makris & Ginzburg, 1987; Prodehl et al., 1997) and supports the hypothesis that most of the Afar crust includes a significant component of solidified mafic rock (Furman et al., 2006). Afar also appears fast in depth sections that cut through the Afar mantle, consistent with faster velocities for mantle peridotite than crustal rocks. This is especially noticeable beneath the Danakil Depression, where particularly thin crust (~16-km thick; Berckhemer et al., 1975; Hammond et al., 2011), significantly reduces the depth of the mantle compared to other regions (Figure 6a "c").

An exception to the fast Afar crust is a region of slower velocities broadly beneath the magmatic segments (Figures 6a–6d "b"), down to 3.45 ± 0.04 km/s at a depth of 10 km and 3.85 ± 0.06 km/s at a depth of 40 km. This is most clearly evident at the Dabbahu and Hararo magmatic segments, the location of the 2005–2010 Dabbahu dyking event (Ebinger et al., 2010; Grandin et al., 2012; Illsley-Kemp et al., 2018). Previous studies also find slow velocities (Korostelev et al., 2015; Stork et al., 2013) and high conductivities (Desissa et al., 2013; Johnson et al., 2015), which have been used to estimate a 500-km^3 melt body with 13% melt beneath this region associated with the dyking event (Desissa et al., 2013). Slow velocities coupled with the recent dyking event suggest we image melt associated with the event. We see a similar slow velocity zone beneath the Nabro volcanic chain which erupted in 2011 (Goitom et al., 2015) suggesting we are again imaging hotter crust and partial melt in the crust.

6.2.3. Comparison of the MER to Afar

The transition from the MER into Afar is marked by a distinct 5% increase in velocity where the rift widens into Afar. Both areas have had recent volcanic eruptions (Hutchison et al., 2016; Macgregor, 2015; Wadge et al., 2016) but Afar has more rapid melt extraction to the near surface (e.g., the Erta Ale lava lake, 2008 Alu-Dalafilla eruption, and the 2005 Dabbahu dyking event). Afar is extending 3–4 times faster than the MER (Keir et al., 2013), and we would therefore expect higher rates of melt production beneath Afar (Rooney, 2010; Rooney et al., 2005). We do not observe a correlation between slow *Vs* and predicted total rates of melt production and volcanism. Instead, we observe slow *Vs* in parts of the rift valley with the lowest surface expression of recent basaltic type volcanism, suggesting that time scales of melt storage plays an important role in controlling *Vs*. Petrological studies of the two regions find the most chemically evolved compositions are associated with volcanoes of the MER (Hutchison et al., 2018; Rooney et al., 2013). In Afar, the on-axis segments produce less evolved melts while at Erta Ale, the most advanced stage of rifting, there is little evidence for melt evolution and assimilation (Hutchison et al., 2018). Our observations of slow velocities in the MER is consistent with petrological constraints that the residence time of melts is longer during the earlier stages of rifting. Longer melt residence times would allow greater melt accumulation as more melt is added but not erupted and would heat the surrounding crust. Both effects would reduce seismic velocities.

Melt accumulation beneath the MER may also be aided by thicker crust and a narrow rift (Bastow et al., 2008; Debayle et al., 2001; Faccenna et al., 2008; Gallacher et al., 2016), coupled with significant changes in lithospheric structure which could act to focus melt beneath the rift (Dugda et al., 2005; Hammond et al., 2011; Stuart et al., 2006). We therefore propose 3-D melt focusing coupled with longer residence times of melt within the crust of the MER to explain the slowest velocities of our study.

6.2.4. The Northwestern and Southeastern Plateaus

The plateaus display greater heterogeneity than the MER and Afar. The velocities are predominantly fast beneath the plateaus, typically around 3.65 ± 0.05 km/s at 10-km depth and ~3.95 ± 0.07 km/s at 40-km depth (Figures 6a–6d and 8b "e" and "f"). The southeastern plateau has limited recent volcanism suggesting it has not been modified by melt. Therefore, the southeastern plateau may represent the background velocity of the region. Further evidence for limited melt is corroborated by *Vp*/*Vs* ratios of ~1.78 and highly resistive crust (Hammond et al., 2011; Whaler & Hautot, 2006).

In contrast to the southeastern plateau, we observe localized regions with slow velocities of 3.25 ± 0.05 km/s at 10 km going down to 3.65 ± 0.07 km/s at 30-km depth beneath the northwestern plateau (Figures 6a–6c

and 8b "d"). At the surface, "d" underlies the Choke and Guguftu shield volcanoes which last erupted 22 Ma (Kieffer et al., 2004; Pik et al., 1998, 1999), timescales over which melt would no longer be present due to cooling. One anomaly follows the trend of the border faults and known geothermal activity (Figures 6a–6d), suggesting fluids and geothermal circulation in the fault system may be responsible for the slow *Vs* anomalies. This was also observed by Korostelev et al. (2015), who drew a link with geothermal activity and slow velocities.

The slow anomaly west of the border faults at "d" may have a similar origin. On either side of the flood basalts are northwest–southeast trending faults. On the southeastern plateau we have the Ogaden rift (Figure 1b) and on the northwestern plateau are the Blue Nile and Atbara Rifts (Mège & Korme, 2004). It is likely that these failed rifts underlie the Ethiopian flood basalts and could produce similar geothermal systems to those of the border faults. Surface evidence of fumaroles and geothermal activity is present in this region (Keir et al., 2009) particularly at the southeastern edge of lake Tana (Figures 6a–6d). These geothermal systems indicate that there are continuous intrusions beneath this region or ongoing conductive cooling leading to the release of volatiles. We therefore propose that slow velocities beneath the plateau at "d" are generated by geothermal systems with fluids migrating through large-scale fault structures (Keir et al., 2009). The slow velocity zones also correlate well with high conductivities from magnetotelluric studies (Hautot et al., 2006; Whaler & Hautot, 2006) and perhaps link to geothermal activity at the border faults (Korostelev et al., 2015). In contrast, the slow velocities of 3.30 ± 0.05 km/s beneath the Yemen plateau (Figures 6a, 6b, and 8a) correlate well with the active Harras of Dhamar volcanic field (Korostelev et al., 2015).

6.2.5. Implications for Magma Plumbing Systems During Continental Rifting

Our absolute shear velocity models provide evidence for more protracted melt storage in the crust during the earlier stages of rifting (e.g., the MER). Melt accumulation is particularly localized near the Moho but distributed spatially across a relatively broad region beneath the rift valley and surrounding plateaus. This contributes to the growing body of evidence that deep crustal magma complexes play an important role in the evolution of magma in continental rifts (Annen et al., 2006). Controlled source imaging of continental rifts (e.g., The Baikal rift; Thybo & Nielsen, 2009) and magmatic passive margins (e.g., the North Atlantic; White et al., 2008) suggest that melt is primarily arranged as complexes of stacked sills. The accumulation of melt is aided by strong density contrasts of the higher rigidity continental crust overlying weaker mantle (Bradley, 1965; Kavanagh et al., 2006).

In Afar, we observe faster crustal seismic velocities mostly consistent with a crust rich in frozen mafic rock, denser than continental crust. The ascent of melt through the crust primarily relies on its high buoyancy relative to the mantle and crust (Harmon & Rychert, 2015; Sawyer, 1994). The time accumulation of dense mafic intrusion during progressive rifting, coupled with ongoing crustal thinning likely aids melt ascent through the crust during continued continental breakup in contrast to the thicker crust of the Ethiopian plateau and MER. Such an interpretation satisfies our seismic images, as well as petrological constraints on magma residence times (Hutchison et al., 2018).

Our seismic images beneath the northwestern plateau suggest localized melt emplacement and related hydrothermal processes continuing outside of the rift valley to the present day. This interpretation is somewhat contrary to the widely held belief that all magmatism becomes localized to a rift valley during progressive rifting. New GPS constraints from Ethiopia showing the presence of ongoing extension of the plateau (Birhanu et al., 2016) provides a mechanism to explain recent magmatic processes here and supports the view that extension coupled with magmatism may remain distributed later into the breakup process than previously believed.

7. Conclusions

We have generated a 3-D absolute shear wave velocity map for the crust and uppermost mantle of the northern EAR. This unified model allows direct comparisons of shear velocity between the MER, Afar, and adjacent plateaus. We have used 170 seismic stations to produce 4,820 cross correlations which have been stacked and inverted for phase and shear velocity on a 0.25° × 0.25° nodal grid. Shear velocities range from 3.20–4.10 km/s with the slowest average velocities within the MER (3.60 ± 0.03 km/s) and fastest beneath the Danakil depression (3.83 ± 0.04 km/s). The key findings of our study are

1. Mantle velocities (3.60–4.10 km/s) are everywhere slower than the global average for a mantle peridotite composition and require moderate elevated temperatures combined with a fluid component and/or partial melt
2. Average shear velocities for the MER (3.60 ± 0.03 km/s) are slower than Afar (3.83 ± 0.04 km/s). Slow velocities in the MER versus Afar are interpreted as melt focusing from dramatic changes in lithospheric topography coupled with longer residence times and complex magmatic pathways within the crust. Faster velocities within Afar are attributed to solidified crustal intrusions and isolated areas of melt too small to be imaged in this study.
3. The Ethiopian plateau displays heterogeneity in crustal velocity structure (3.25 ± 0.05 km/s at 10-km depth to 3.87 ± 0.07 km/s at 40-km depth at "d" and 3.65 ± 0.05 km/s at 10-km depth to 3.95 ± 0.065 km/s at 40-km depth at "e"), suggesting a complex geological history and an inhomogeneous magma distribution during evolution. Slower crustal velocities near the border fault regions and pre-existing failed rifts are interpreted as geothermal systems within the faults beneath the Ethiopian flood basalts.

Acknowledgments
E. L. C is funded through NERC studentship NE/L002531/1. D. K. is supported by NERC grant NE/L013932. C. A. R. and N. H. acknowledge funding from the Natural Environment Research Council (NE/M003507/1 and NE/K010654/1) and the European Research Council (GA 638665). All data needed to generate these models are freely available from the IRIS Data Management Center (IRISDMC; https://service.iris.edu/fdsnws/dataselect/1/). IRIS Data Services are funded through the Seismological Facilities for the Advancement of Geoscience and EarthScope (SAGE) Proposal of the National Science Foundation under Cooperative Agreement EAR-126168. We thank SEIS-UK for use of the instruments and their computing facilities. The facilities of SEIS-UK are supported by the Natural Environment Research Council (NERC) under agreement R8/H10/64. F. Some figures were made using the Generic Mapping Tools (Wessel et al., 2013).

References

Annen, C., Blundy, J. D., & Sparks, R. S. J. (2006). The genesis of intermediate and silicic magmas in deep crustal hot zones. *Journal of Petrology*, *47*(3), 505–539. https://doi.org/10.1093/petrology/egi084

Armitage, J. J., Ferguson, D. J., Goes, S., Hammond, J. O. S., Calais, E., Rychert, C. A., & Harmon, N. (2015). Upper mantle temperature and the onset of extension and break-up in Afar, Africa. *Earth and Planetary Science Letters*, *418*, 78–90. https://doi.org/10.1016/j.epsl.2015.02.039

Armitage, J. J., Petersen, K. D., & Pérez-Gussinyé, M. (2018). The role of crustal strength in controlling magmatism and melt chemistry during rifting and break-up. *Geochemistry, Geophysics, Geosystems*, *19*, 534–550. https://doi.org/10.1002/2017GC007326

Ayele, A., Stuart, G. W., & Kendall, J.-M. (2004). Insights into rifting from shear wave splitting and receiver functions: An example from Ethiopia. *Geophysical Journal International*, *157*(1), 354–362. https://doi.org/10.1111/j.1365-246X.2004.02206.x

Barnie, T. D., Keir, D., Hamling, I., Hofmann, B., Belachew, M., Carn, S., et al. (2016). A multidisciplinary study of the final episode of the Manda Hararo dyke sequence, Ethiopia, and implications for trends in volcanism during the rifting cycle. *Geological Society, London, Special Publications*, *420*(1), 149–163. https://doi.org/10.1144/SP420.6

Bastow, I. D., Keir, D., & Daly, E. (2011). The Ethiopia Afar Geoscientific Lithospheric Experiment (EAGLE): Probing the transition from continental rifting to incipient seafloor spreading. *The Geological Society of America Special Papers*, *478*, 51–76. https://doi.org/10.1130/2011.2478(04)

Bastow, I. D., Nyblade, A. A., Stuart, G. W., Rooney, T. O., & Benoit, M. H. (2008). Upper mantle seismic structure beneath the Ethiopian hot spot: Rifting at the edge of the African low-velocity anomaly. *Geochemistry, Geophysics, Geosystems*, *9*, Q12022. https://doi.org/10.1029/2008GC002107

Bastow, I. D., Stuart, G. W., Kendall, J.-M., & Ebinger, C. J. (2005). Upper-mantle seismic structure in a region of incipient continental breakup: Northern Ethiopian rift. *Geophysical Journal International*, *162*(2), 479–493. https://doi.org/10.1111/j.1365-246X.2005.02666.x

Beccaluva, L., Bianchini, G., Natali, C., & Siena, F. (2009). Continental flood basalts and mantle plumes: A case study of the northern Ethiopian plateau. *Journal of Petrology*, *50*(7), 1377–1403. https://doi.org/10.1093/petrology/egp024

Bensen, G. D., Ritzwoller, M. H., Barmin, M. P., Levshin, A. L., Lin, F., Moschetti, M. P., et al. (2007). Processing seismic ambient noise data to obtain reliable broad-band surface wave dispersion measurements. *Geophysical Journal International*, *169*(3), 1239–1260. https://doi.org/10.1111/j.1365-246X.2007.03374.x

Berckhemer, H., Baier, B., Bartelsen, H., Behle, A., Burkhardt, H., Gebrande, H., et al. (1975). Deep seismic soundings in the Afar region and on the highland of Ethiopia. In A. Pilger & A. Rosler (Eds.), *Afar Depression of Ethiopia* (pp. 89–107). Stuttgart: E. Schweizerbart'sche Verlagsbuchhandlung.

Berhe, S. (1990). Ophiolites in Northeast and East Africa: Implications Proterozoic crustal growth. *Journal of the Geological Society of London*, *147*(1), 41–57. https://doi.org/10.1144/gsjgs.147.1.0041

Biggs, J., Bastow, I. D., Keir, D., & Lewi, E. (2011). Pulses of deformation reveal frequently recurring shallow magmatic activity beneath the Main Ethiopian Rift. *Geochemistry, Geophysics, Geosystems*, *12*, Q0AB10. https://doi.org/10.1029/2011GC003662

Bilham, R., Bendick, R., Larson, K., Mohr, P., Braun, J., Tesfaye, S., & Asfaw, L. (1999). Secular and tidal strain across the Main Ethiopian Rift. *Geophysical Research Letters*, *26*(18), 2789–2792. https://doi.org/10.1029/1998GL005315

Birch, F. (1960). The velocity of compressional waves in rocks to 10 kilobars, part 1. *Journal of Geophysical Research*, *65*(4), 1083–1102. https://doi.org/10.1029/JZ065i004p01083

Birhanu, Y., Bendick, R., Fisseha, S., Lewi, E., Floyd, M., King, R., & Reilinger, R. (2016). GPS constraints on broad scale extension in the Ethiopian Highlands and Main Ethiopian Rift. *Geophysical Research Letters*, *43*, 6844–6851. https://doi.org/10.1002/2016GL069890

Bonatti, E. (1985). Punctiform initiation of seafloor spreading in the Red Sea during transition from a continental to an oceanic rift. *Nature*, *316*(6023), 33–37. https://doi.org/10.1038/316033a0

Bosworth, W., Huchon, P., & McClay, K. (2005). The Red Sea and Gulf of Aden basins. *Journal of African Earth Sciences*, *43*(1–3), 334–378. https://doi.org/10.1016/j.jafrearsci.2005.07.020

Braathen, A., Grenne, T., Selassie, M. G., & Worku, T. (2001). Juxtaposition of Neoproterozoic units along the Baruda—Tulu Dimtu shear-belt in the east African Orogen of western Ethiopia. *Precambrian Research*, *107*(3-4), 215–234. https://doi.org/10.1016/S0301-9268(00)00143-1

Bradley, J. (1965). Intrusions of major dolerite sills. *Transactions of the Royal Society of New Zealand*, *3*(4), 27–55.

Buck, W. R. (2004). Consequences of asthenospheric variability on continental rifting. In G. Karner, B. Taylor, N. Driscoll, & D. Kohlstedt (Eds.), *Rheology and deformation of the lithosphere at continental margins* (pp. 1–31). New York, Chichester: Columbia University Press. https://doi.org/10.7312/karn12738-002

Buck, W. R. (2006). The role of magma in the development of the Afro-Arabian Rift system. *Geological Society, London, Special Publications*, *259*(1), 43–54. https://doi.org/10.1144/GSL.SP.2006.259.01.05

Caricchi, L., Burlini, L., & Ulmer, P. (2008). Propagation of *P* and *S*-waves in magmas with different crystal contents: Insights into the crystallinity of magmatic reservoirs. *Journal of Volcanology and Geothermal Research*, *178*(4), 740–750. https://doi.org/10.1016/j.jvolgeores.2008.09.006

Casey, M., Ebinger, C. J., Keir, D., Gloaguen, R., & Mohamed, F. (2006). Strain accommodation in transitional rifts: Extension by magma intrusion and faulting in Ethiopian rift magmatic segments. *Geological Society, London, Special Publications*, *259*(1), 143–163. https://doi.org/10.1144/GSL.SP.2006.259.01.13

Christensen, N. I. (1996). Poisson's ratio and crustal seismology. *Journal of Geophysical Research*, *101*(B2), 3139–3156. https://doi.org/10.1029/95JB03446

Civiero, C., Goes, S., Hammond, J. O. S., Fishwick, S., Ahmed, A., Ayele, A., et al. (2016). Small-scale thermal upwellings under the northern East African rift froms travel time tomography. *Journal of Geophysical Research: Solid Earth*, *121*, 7395–7408. https://doi.org/10.1002/2016JB013070

Civiero, C., Hammond, J. O. S., Goes, S., Fishwick, S., Ahmed, A., Ayele, A., et al. (2015). Multiple mantle upwellings in the transition zone beneath the northern east-African rift system from relative *P*-wave travel-time tomography. *Geochemistry, Geophysics, Geosystems*, *16*, 2949–2968. https://doi.org/10.1002/2015GC005948

Cornwell, D. G., Mackenzie, G. D., England, R. W., Maguire, P. K. H., Asfaw, L., & Oluma, B. (2006). Northern Main Ethiopian Rift crustal structure from new high-precision gravity data. *Geological Society, London, Special Publications*, *259*(1), 307–321. https://doi.org/10.1144/GSL.SP.2006.259.01.23

Cornwell, D. G., Maguire, P. K. H., England, R. W., & Stuart, G. W. (2010). Imaging detailed crustal structure and magmatic intrusion across the Ethiopian Rift using a dense linear broadband array. *Geochemistry, Geophysics, Geosystems*, *11*, Q0AB03. https://doi.org/10.1029/2009GC002637

Corti, G. (2009). Continental rift evolution: From rift initiation to incipient break-up in the Main Ethiopian Rift, East Africa. *Earth-Science Reviews*, *96*(1–2), 1–53. https://doi.org/10.1016/j.earscirev.2009.06.005

Corti, G., Philippon, M., Sani, F., Keir, D., & Kidane, T. (2013). Re-orientation of the extension direction and pure extensional faulting at oblique rift margins: Comparison between the Main Ethiopian Rift and laboratory experiments. *Terra Nova*, *25*(5), 396–404. https://doi.org/10.1111/ter.12049

Debayle, E., Lévêque, J. J., & Cara, M. (2001). Seismic evidence for a deeply rooted low-velocity anomaly in the upper mantle beneath the northeastern afro/Arabian continent. *Earth and Planetary Science Letters*, *193*(3–4), 423–436. https://doi.org/10.1016/S0012-821X(01)00509-X

Desissa, M., Johnson, N. E., Whaler, K. A., Hautot, S., Fisseha, S., & Dawes, G. J. K. (2013). A mantle magma reservoir beneath an incipient mid-ocean ridge in Afar, Ethiopia. *Nature Geoscience*, *6*(10), 861–865. https://doi.org/10.1038/ngeo1925

Dugda, M. T., & Nyblade, A. A. (2006). New constraints on crustal structure in eastern Afar from the analysis of receiver functions and surface wave dispersion in Djibouti. *Afar Volcanic Province within the East African Rift System*, *259*, 239–251. https://doi.org/10.1144/gsl.sp.2006.259.01.19

Dugda, M. T., Nyblade, A. A., Julia, J., Langston, C. A., Ammon, C. J., & Simiyu, S. (2005). Crustal structure in Ethiopia and Kenya from receiver function analysis: Implications for rift development in eastern Africa. *Journal of Geophysical Research*, *110*, B01303. https://doi.org/10.1029/2004JB003065

Ebinger, C. J., Ayele, A., Keir, D., Rowland, J., Yirgu, G., Wright, T., et al. (2010). Length and timescales of rift faulting and magma intrusion: The Afar rifting cycle from 2005 to present. *Annual Review of Earth and Planetary Sciences*, *38*(1), 439–466. https://doi.org/10.1146/annurev-earth-040809-152333

Ebinger, C. J., & Casey, M. (2001). Continental breakup in magmatic provinces: An Ethiopian example. *Geology*, *29*(6), 527–530. https://doi.org/10.1130/0091-7613(2001)029<0527:CBIMPA>2.0.CO;2

Ebinger, C. J., Yemane, T., Harding, D. J., Tesfaye, S., Kelley, S., & Rex, D. C. (2000). Rift deflection, migration, and propagation: Linkage of the Ethiopian and eastern rifts, Africa. *Bulletin of the Geological Society of America*, *112*(2), 163–176. https://doi.org/10.1130/0016-7606(2000)112<163:RDMAPL>2.0.CO;2

Ebinger, C. J., Yemane, T., WoldeGabriel, G., Aronson, J. L., & C., W. R. (1993). Late Eocene-recent volcanism and faulting in the southern main Ethiopian rift. *Journal of the Geological Society of London*, *150*(1), 99–108. https://doi.org/10.1144/gsjgs.150.1.0099

Faccenna, C., Rossetti, F., Becker, T. W., Danesi, S., & Morelli, A. (2008). Recent extension driven by mantle upwelling beneath the Admiralty Mountains (East Antarctica). *Tectonics*, *27*, TC4015. https://doi.org/10.1029/2007TC002197

Faul, U. H., & Jackson, I. (2005). The seismological signature of temperature and grain size variations in the upper mantle. *Earth and Planetary Science Letters*, *234*(1-2), 119–134. https://doi.org/10.1016/j.epsl.2005.02.008

Ferguson, D. J., Maclennan, J., Bastow, I. D., Pyle, D. M., Jones, S. M., Keir, D., et al. (2013). Melting during late-stage rifting in Afar is hot and deep. *Nature*, *499*(7456), 70–73. https://doi.org/10.1038/nature12292

Fishwick, S. (2010). Surface wave tomography: Imaging of the lithosphere-asthenosphere boundary beneath central and southern Africa? *Lithos*, *120*(1–2), 63–73. https://doi.org/10.1016/j.lithos.2010.05.011

Furman, T., Bryce, J., Rooney, T. O., Hanan, B. B., Yirgu, G., & Ayalew, D. (2006). Ethiopian volcanic province. *Geological Society, London, Special Publications*, *259*(1), 95–119. https://doi.org/10.1144/GSL.SP.2006.259.01.09

Gallacher, R. J., Keir, D., Harmon, N., Stuart, G., Leroy, S., Hammond, J. O. S., et al. (2016). The initiation of segmented buoyancy-driven melting during continental breakup. *Nature Communications*, *7*(1), 13110. https://doi.org/10.1038/ncomms13110

Gao, H. (2016). Seismic velocity structure of the Juan de Fuca and Gorda plates revealed by a joint inversion of ambient noise and regional earthquakes. *Geophysical Research Letters*, *43*, 5194–5201. https://doi.org/10.1002/2016GL069381

Goitom, B., Oppenheimer, C., Hammond, J. O. S., Grandin, R., Barnie, T., Donovan, A., et al. (2015). First recorded eruption of Nabro volcano, Eritrea, 2011. *Bulletin of Volcanology*, *77*(10), 85. https://doi.org/10.1007/s00445-015-0966-3

Grandin, R., Jacques, E., Nercessian, A., Ayele, A., Doubre, C., Socquet, A., et al. (2012). Seismicity during lateral dike propagation: Insights from new data in the recent Manda Hararo-Dabbahu rifting episode (Afar, Ethiopia). *Geochemistry, Geophysics, Geosystems*, *12*, Q0AB08. https://doi.org/10.1029/2010GC003434

Guidarelli, M., Stuart, G. W., Hammond, J. O. S., Kendall, J.-M., Ayele, A., & Belachew, M. (2011). Surface wave tomography across Afar, Ethiopia: Crustal structure at a rift triple-junction zone. *Geophysical Research Letters*, *38*, L24313. https://doi.org/10.1029/2011GL046840

Hacker, B. R., & Abers, G. A. (2004). Subduction Factory 3: An Excel worksheet and macro for calculating the densities, seismic wave speeds, and H_2O contents of minerals and rocks at pressure and temperature. *Geochemistry, Geophysics, Geosystems*, *5*, Q01005. https://doi.org/10.1029/2003GC000614

Hammond, J. O. S. (2014). Constraining melt geometries beneath the Afar depression, Ethiopia from teleseismic receiver functions: The anisotropic H-k stacking technique. *Geochemistry, Geophysics, Geosystems*, *15*, 1316–1332. https://doi.org/10.1002/2013GC005186

Hammond, J. O. S., & Kendall, J.-M. (2016). Constraints on melt distribution from seismology: A case study in Ethiopia. *Geological Society, London, Special Publications*, *420*(1), 127–147. https://doi.org/10.1144/SP420.14

Hammond, J. O. S., Kendall, J.-M., Stuart, G. W., Ebinger, C. J., Bastow, I. D., Keir, D., et al. (2013). Mantle upwelling and initiation of rift segmentation beneath the Afar depression. *Geology*, *41*(6), 635–638. https://doi.org/10.1130/G33925.1

Hammond, J. O. S., Kendall, J.-M., Stuart, G. W., Keir, D., Ebinger, C. J., Ayele, A., & Belachew, M. (2011). The nature of the crust beneath the Afar triple junction: Evidence from receiver functions. *Geochemistry, Geophysics, Geosystems*, *12*, Q12004. https://doi.org/10.1029/2011GC003738

Hammond, J. O. S., Kendall, J.-M., Wookey, J., Stuart, G. W., Keir, D., & Ayele, A. (2014). Differentiating flow, melt, or fossil seismic anisotropy beneath Ethiopia. *Geochemistry, Geophysics, Geosystems*, *15*, 1878–1894. https://doi.org/10.1002/2013GC005185

Hammond, W. C., & Humphreys, E. D. (2000). Upper mantle seismic wave attenuation: Effects of realistic partial melt distribution. *Journal of Geophysical Research*, *105*, 10,987–10,999. https://doi.org/10.1029/2000JB900042

Harmon, N., De La Cruz, M. S., Rychert, C. A., Abers, G. A., & Fischer, K. M. (2013). Crustal and mantle shear velocity structure of Costa Rica and Nicaragua from ambient noise and teleseismic Rayleigh wave tomography. *Geophysical Journal International*, *195*(2), 1300–1313. https://doi.org/10.1093/gji/ggt309

Harmon, N., Forsyth, D. W., & Webb, S. C. (2007). Using ambient seismic noise to determine short-period phase velocities and shallow shear velocities in young oceanic lithosphere. *Bulletin of the Seismological Society of America*, *97*(6), 2009–2023. https://doi.org/10.1785/0120070050

Harmon, N., Forsyth, D. W., & Weeraratne, D. S. (2009). Thickening of young Pacific lithosphere from high-resolution Rayleigh wave tomography: A test of the conductive cooling model. *Earth and Planetary Science Letters*, *278*(1–2), 96–106. https://doi.org/10.1016/j.epsl.2008.11.025

Harmon, N., Gerstoft, P., Rychert, C. A., Abers, G. A., De La Cruz, M. S., & Fischer, K. M. (2008). Phase velocities from seismic noise using beamforming and cross correlation in Costa Rica and Nicaragua. *Geophysical Research Letters*, *35*, L19303. https://doi.org/10.1029/2008GL035387

Harmon, N., Rychert, C., & Gerstoft, P. (2010). Distribution of noise sources for seismic interferometry. *Geophysical Journal International*, *183*(3), 1470–1484. https://doi.org/10.1111/j.1365-246x.2010.04802.x

Harmon, N., & Rychert, C. A. (2015). Seismic imaging of deep crustal melt sills beneath Costa Rica suggests a method for the formation of the Archean continental crust. *Earth and Planetary Science Letters*, *430*, 140–148. https://doi.org/10.1016/j.epsl.2015.07.062

Harmon, N., & Rychert, C. A. (2016). Joint inversion of teleseismic and ambient noise Rayleigh waves for phase velocity maps, an application to Iceland. *Journal of Geophysical Research: Solid Earth*, *121*, 5966–5987. https://doi.org/10.1002/2016JB012934

Hautot, S., Whaler, K. A., Gebru, W., & Desissa, M. (2006). The structure of a Mesozoic basin beneath the Lake Tana area, Ethiopia, revealed by magnetotelluric imaging. *Journal of African Earth Sciences*, *44*(3), 331–338. https://doi.org/10.1016/j.jafrearsci.2005.11.027

Havlin, C., Parmentier, E. M., & Hirth, G. (2013). Dike propagation driven by melt accumulation at the lithosphere—Asthenosphere boundary. *Earth and Planetary Science Letters*, *376*, 20–28. https://doi.org/10.1016/j.epsl.2013.06.010

Hayward, N. J., & Ebinger, C. J. (1996). Variations in the along-axis segmentation of the Afar rift system. *Tectonics*, *15*(2), 244–257. https://doi.org/10.1029/95TC02292

Hofmann, C., Courtillot, V., Féraud, G., Rochette, P., Yirgu, G., Ketefo, E., & Pik, R. (1997). Timing of the Ethiopian flood basalt event and implications for plume birth and global change. *Nature*, *389*(6653), 838–841. https://doi.org/10.1038/39853

Holtzman, B. K., & Kendall, J.-M. (2010). Organized melt, seismic anisotropy, and plate boundary lubrication. *Geochemistry, Geophysics, Geosystems*, *11*, Q0AB06. https://doi.org/10.1029/2010GC003296

Hutchison, W., Biggs, J., Mather, T. A., Pyle, D. M., Lewi, E., Yirgu, G., et al. (2016). Causes of unrest at silicic calderas in the East African Rift: New constraints from InSAR and soil-gas chemistry at Aluto volcano, Ethiopia. *Geochemistry, Geophysics, Geosystems*, *17*, 3008–3030. https://doi.org/10.1002/2016GC006395

Hutchison, W., Mather, T. A., Pyle, D. M., Biggs, J., & Yirgu, G. (2015). Structural controls on fluid pathways in an active rift system: A case study of the Aluto volcanic complex. *Geosphere*, *11*(3), 542–562. https://doi.org/10.1130/GES01119.1

Hutchison, W., Mather, T. A., Pyle, D. M., Boyce, A. J., Gleeson, M. L. M., Yirgu, G., et al. (2018). The evolution of magma during continental rifting: New constraints from the isotopic and trace element signatures of silicic magmas from Ethiopian volcanoes. *Earth and Planetary Science Letters*, *489*, 203–218. https://doi.org/10.1016/j.epsl.2018.02.027

Illsley-Kemp, F., Keir, D., Bull, J. M., Gernon, T. M., Ebinger, C., Ayele, A., et al. (2018). Seismicity during continental breakup in the Red Sea rift of northern Afar. *Journal of Geophysical Research: Solid Earth*, *123*, 2345–2362. https://doi.org/10.1002/2017JB014902

Jackson, I., & Faul, U. H. (2010). Grainsize-sensitive viscoelastic relaxation in olivine: Towards a robust laboratory-based model for seismological application. *Physics of the Earth and Planetary Interiors*, *183*(1–2), 151–163. https://doi.org/10.1016/j.pepi.2010.09.005

Jestin, F., Huchon, P., & Gaulier, J. M. (1994). The Somalia plate and the East-African Rift system—Present-day kinematics. *Geophysical Journal International*, *116*(3), 637–654. https://doi.org/10.1111/j.1365-246X.1994.tb03286.x

Johnson, N. E., Whaler, K. A., Hautot, S., Fisseha, S., Desissa, M., & Dawes, G. J. K. (2015). Magma imaged magnetotellurically beneath an active and an inactive magmatic segment in Afar, Ethiopia. *Geological Society, London, Special Publications*, *14*, 150000. https://doi.org/10.1144/SP420.11

Karato, S. I. (2004). Mapping water content in the upper mantle. *Geophysical Monograph Series*, *138*, 135–152. https://doi.org/10.1029/138GM08

Kavanagh, J. L., Menand, T., & Sparks, R. S. J. (2006). An experimental investigation of sill formation and propagation in layered elastic media. *Earth and Planetary Science Letters*, *245*(3–4), 799–813. https://doi.org/10.1016/j.epsl.2006.03.025

Kazmin, V., Shifferaw, A., & Balcha, T. (1978). The Ethiopian basement: Stratigraphy and possible manner of evolution. *Geologische Rundschau*, *67*(2), 531–546. https://doi.org/10.1007/BF01802803

Keir, D., Bastow, I. D., Pagli, C., & Chambers, E. L. (2013). The development of extension and magmatism in the Red Sea rift of Afar. *Tectonophysics*, *607*, 98–114. https://doi.org/10.1016/j.tecto.2012.10.015

Keir, D., Bastow, I. D., Whaler, K. A., Daly, E., Cornwell, D. G., & Hautot, S. (2009). Lower crustal earthquakes near the Ethiopian rift induced by magmatic processes. *Geochemistry, Geophysics, Geosystems*, *10*, Q0AB02. https://doi.org/10.1029/2009GC002382

Kennett, B. L. N., Engdahl, E. R., & Buland, R. (1995). Constraints on seismic velocities in the Earth from traveltimes. *Geophysical Journal International*, *122*(1), 108–124. https://doi.org/10.1111/j.1365-246X.1995.tb03540.x

Keranen, K. M., & Klemperer, S. L. (2008). Discontinuous and diachronous evolution of the Main Ethiopian Rift: Implications for development of continental rifts. *Earth and Planetary Science Letters*, *265*(1–2), 96–111. https://doi.org/10.1016/j.epsl.2007.09.038

Keranen, K. M., Klemperer, S. L., Gloaguen, R., & EAGLE Working Group (2004). Three-dimensional seismic imaging of a protoridge axis in the Main Ethiopian Rift. *Geology*, *32*(11), 949–952. https://doi.org/10.1130/G20737.1

Keranen, K. M., Klemperer, S. L., Julia, J., Lawrence, J. F., & Nyblade, A. A. (2009). Low lower crustal velocity across Ethiopia: Is the Main Ethiopian Rift a narrow rift in a hot craton? *Geochemistry, Geophysics, Geosystems*, *10*, Q0AB01. https://doi.org/10.1029/2008GC002293

Kieffer, B., Arndt, N., Lapierre, H., Bastien, F., Bosch, D., Pecher, A., et al. (2004). Flood and shield basalts from Ethiopia: Magmas from the African superswell. *Journal of Petrology*, *45*(4), 793–834. https://doi.org/10.1093/petrology/egg112

Kim, S., Nyblade, A. A., Rhie, J., Baag, C.-E., & Kang, T.-S. (2012). Crustal *S*-wave velocity structure of the Main Ethiopian Rift from ambient noise tomography. *Geophysical Journal International*, *191*(2), 865–878. https://doi.org/10.1111/j.1365-246X.2012.05664.x

Korostelev, F., Weemstra, C., Leroy, S., Boschi, L., Keir, D., Ren, Y., et al. (2015). Magmatism on rift flanks: Insights from ambient noise phase velocity in Afar region. *Geophysical Research Letters*, *42*, 2179–2188. https://doi.org/10.1002/2015GL063259

Laske, G., Masters, G., Ma, Z., & Pasyanos, M. (2013). Update on CRUST1.0—A 1-degree global model of Earth's crust. EGU General Assembly 2013, 15, 2658. Retrieved from. https://meetingorganizer.copernicus.org/EGU2013/EGU2013-2658.pdf

Lavayssiere, A., Rychert, C. A., Harmon, N., Keir, D., Hammond, J. O. S., Kendall, J.-M., et al. (2018). Imaging lithospheric discontinuities beneath the northern East African Rift using *S*-to-*P* receiver functions. *Geochemistry, Geophysics, Geosystems*, *19*, 4048–4062. https://doi.org/10.1029/2018GC007463

Lee, C.-T. A. (2003). Compositional variation of density and seismic velocities in natural peridotites at STP conditions: Implications for seismic imaging of compositional heterogeneities in the upper mantle. *Journal of Geophysical Research*, *108*(B9), 2441. https://doi.org/10.1029/2003JB002413

Macgregor, D. (2015). History of the development of the east African Rift System: A series of interpreted maps through time. *Journal of African Earth Sciences*, *101*, 232–252. https://doi.org/10.1016/j.jafrearsci.2014.09.016

Mackenzie, G. D., Thybo, H., & Maguire, P. K. H. (2005). Crustal velocity structure across the Main Ethiopian Rift: Results from two-dimensional wide-angle seismic modelling. *Geophysical Journal International*, *162*(3), 994–1006. https://doi.org/10.1111/j.1365-246X.2005.02710.x

Magee, C., Muirhead, J. D., Karvelas, A., Holford, S. P., Jackson, C. A. L., Bastow, I. D., et al. (2016). Lateral magma flow in mafic sill complexes. *Geosphere*, *12*(3), 809–841. https://doi.org/10.1130/GES01256.1

Maguire, P. K. H., Keller, G. R., Klemperer, S. L., Mackenzie, G. D., Keranen, K., Harder, S., et al. (2006). Crustal structure of the northern Main Ethiopian Rift from the EAGLE controlled-source survey; A snapshot of incipient lithospheric break-up. *Geological Society, London, Special Publications*, *259*(1), 269–292. https://doi.org/10.1144/GSL.SP.2006.259.01.21

Makris, J., & Ginzburg, A. (1987). The Afar depression: Transition between continental rifting and sea-floor spreading. *Tectonophysics*, *141*(1–3), 199–214. https://doi.org/10.1016/0040-1951(87)90186-7

Mazzarini, F., Keir, D., & Isola, I. (2013). Spatial relationship between earthquakes and volcanic vents in the central-northern Main Ethiopian Rift. *Journal of Volcanology and Geothermal Research*, *262*, 123–133. https://doi.org/10.1016/j.jvolgeores.2013.05.007

McClusky, S., Reilinger, R., Ogubazghi, G., Amleson, A., Healeb, B., Vernant, P., et al. (2010). Kinematics of the southern Red Sea—Afar triple junction and implications for plate dynamics. *Geophysical Research Letters*, *37*, L05301. https://doi.org/10.1029/2009GL041127

McKenzie, D., Davies, D., & Molnar, P. (1970). Plate tectonics of the Red Sea and East Africa. *Nature*, *226*(5242), 243–248. https://doi.org/10.1038/226243a0

Mège, D., & Korme, T. (2004). Dyke swarm emplacement in the Ethiopian large igneous province: Not only a matter of stress. *Journal of Volcanology and Geothermal Research*, *132*(4), 283–310. https://doi.org/10.1016/S0377-0273(03)00318-4

Merla, G., Abbate, E., Canuti, P., Sagri, M., & Tacconi, P. (1973). *Geological map of Ethiopia and Somalia*. Firenze: Consiglio Nazionale delle Ricerche Italy, Stabilimento Poligrafico Fiorentino.

Nishida, K. (2011). Two-dimensional sensitivity kernels for cross-correlation functions of background surface waves. *Comptes Rendus Geoscience*, *343*(8–9), 584–590. https://doi.org/10.1016/j.crte.2011.02.004

Pik, R., Deniel, C., Coulon, C., Yirgu, G., Hofmann, C., & Ayalew, D. (1998). The northwestern Ethiopian plateau flood basalts: Classification and spatial distribution of magma types. *Journal of Volcanology and Geothermal Research*, *81*(1–2), 91–111. https://doi.org/10.1016/S0377-0273(97)00073-5

Pik, R., Deniel, C., Coulon, C., Yirgu, G., & Marty, B. (1999). Isotopic and trace element signatures of Ethiopian flood basalts: Evidence for plume-lithosphere interactions. *Geochimica et Cosmochimica Acta*, *63*(15), 2263–2279. https://doi.org/10.1016/S0016-7037(99)00141-6

Pinzuti, P., Humler, E., Manighetti, I., & Gaudemer, Y. (2013). Petrological constraints on melt generation beneath the Asal Rift (Djibouti) using quaternary basalts. *Geochemistry, Geophysics, Geosystems*, *14*, 2932–2953. https://doi.org/10.1002/ggge.20187

Prodehl, C., Fuchs, K., & Mechie, J. (1997). Seismic-refraction studies of the Afro-Arabian rift system—A brief review. *Tectonophysics*, *278*(1–4), 1–13. https://doi.org/10.1016/S0040-1951(97)00091-7

Rooney, T. O. (2010). Geochemical evidence of lithospheric thinning in the southern Main Ethiopian rift. *Lithos*, *117*(1–4), 33–48. https://doi.org/10.1016/j.lithos.2010.02.002

Rooney, T. O. (2017). The Cenozoic magmatism of East-Africa: Part I—Flood basalts and pulsed magmatism. *Lithos*, *286–287*, 264–301. https://doi.org/10.1016/j.lithos.2017.05.014

Rooney, T. O., Bastow, I. D., Keir, D., Mazzarini, F., Movsesian, E., Grosfils, E. B., et al. (2014). The protracted development of focused magmatic intrusion during continental rifting. *Tectonics*, *33*, 875–897. https://doi.org/10.1002/2013TC003514

Rooney, T. O., Furman, T., Yirgu, G., & Ayalew, D. (2005). Structure of the Ethiopian lithosphere: Xenolith evidence in the Main Ethiopian rift. *Geochimica et Cosmochimica Acta*, *69*(15), 3889–3910. https://doi.org/10.1016/j.gca.2005.03.043

Rooney, T. O., Herzberg, C., & Bastow, I. D. (2012). Elevated mantle temperature beneath East Africa. *Geology*, *40*(1), 27–30. https://doi.org/10.1130/G32382.1

Rooney, T. O., Mohr, P., Dosso, L., & Hall, C. (2013). Geochemical evidence of mantle reservoir evolution during progressive rifting along the western Afar margin. *Geochimica et Cosmochimica Acta*, *102*, 65–88. https://doi.org/10.1016/j.gca.2012.08.019

Rooney, T. O., Nelson, W. R., Ayalew, D., Hanan, B. B., Yirgu, G., & Kappelman, J. (2017). Melting the lithosphere: Metasomes as a source for mantle-derived magmas. *Earth and Planetary Science Letters*, *461*, 105–118. https://doi.org/10.1016/j.epsl.2016.12.010

Rychert, C. A., Hammond, J. O. S., Harmon, N., Michael Kendall, J., Keir, D., Ebinger, C., et al. (2012). Volcanism in the Afar Rift sustained by decompression melting with minimal plume influence. *Nature Geoscience*, *5*(6), 406–409. https://doi.org/10.1038/ngeo1455

Saito, M. (1988). DISPER80: A subroutine package for the calculation of seismic normal-mode solutions. In D. J. Doornbos (Ed.), *Seismological Algorithms: Computational Methods and Computer Programs*, (pp. 293–319). New York: Academic Press.

Saria, E., Calais, E., Stamps, D. S., Delvaux, D., & Hartnady, C. (2014). Present-day kinematics of the East African Rift. *Journal of Geophysical Research: Solid Earth*, *119*, 3584–3600. https://doi.org/10.1002/2013JB010901

Sawyer, E. W. (1994). Melt segregation in the continental-crust. *Geology*, *22*(11), 1019–1022. https://doi.org/10.1130/0091-7613(1994)022<1019:MSITCC>2.3.CO;2

Schutt, D. L., & Lesher, C. E. (2006). Effects of melt depletion on the density and seismic velocity of garnet and spinel lherzolite. *Journal of Geophysical Research*, *111*, B05401. https://doi.org/10.1029/2003JB002950

Shapiro, N. M., & Campillo, M. (2004). Emergence of broadband Rayleigh waves from correlations of the ambient seismic noise. *Geophysical Research Letters*, *31*, L07614. https://doi.org/10.1029/2004GL019491

Shapiro, N. M., Campillo, M., Stehly, L., & Ritzwoller, M. H. (2005). High-resolution surface wave tomography from ambient seismic noise. *Science*, *307*(5715), 1615–1618. https://doi.org/10.1126/science.1108339

Siegburg, M., Gernon, T. M., Bull, J. M., Keir, D., Barfod, D. N., Taylor, R. N., et al. (2018). Geological evolution of the Boset-Bericha volcanic complex, Main Ethiopian Rift: $^{40}Ar/^{39}Ar$ evidence for episodic Pleistocene to Holocene volcanism. *Journal of Volcanology and Geothermal Research*, *351*, 115–133. https://doi.org/10.1016/j.jvolgeores.2017.12.014

Simmons, G. (1964). Velocity of shear waves in rocks to 10 kilobars, 1. *Journal of Geophysical Research*, *69*(6), 1123–1130. https://doi.org/10.1029/JZ069i006p01123

Stork, A., Stuart, G. W., Henderson, C. M., Keir, D., & Hammond, J. O. S. (2013). Uppermost mantle (Pn) velocity model for the Afar region, Ethiopia: An insight into rifting processes. *Geophysical Journal International*, *193*(1), 321–328. https://doi.org/10.1093/gji/ggs106

Stuart, G. W., Bastow, I. D., & Ebinger, C. J. (2006). Crustal structure of the northern Main Ethiopian Rift from receiver function studies. *Geological Society, London, Special Publications*, *24*(4), 623–626.

Tarantola, A., & Valette, B. (1982). Generalized nonlinear inverse problems solved using the least squares criterion. *Reviews of Geophysics*, *20*(2), 219–232. https://doi.org/10.1029/RG020i002p00219

Thybo, H., & Nielsen, C. A. (2009). Magma-compensated crustal thinning in continental rift zones. *Nature*, *457*(7231), 873–876. https://doi.org/10.1038/nature07688

Tiberi, C., Ebinger, C. J., Ballu, V., Stuart, G. W., & Oluma, B. (2005). Inverse models of gravity data from the Red Sea-Aden-East African rifts triple junction zone. *Geophysical Journal International*, *163*(2), 775–787. https://doi.org/10.1111/j.1365-246X.2005.02736.x

Tromp, J., Luo, Y., Hanasoge, S. M., & Peter, D. (2010). Noise cross-correlation sensitivity kernels. *Geophysical Journal International*, *183*(2), 791–819. https://doi.org/10.1111/j.1365-246X.2010.04721.x

Ukstins, I. A., Renne, P. R., Wolfenden, E., Baker, J., Ayalew, D., & Menzies, M. (2002). Matching conjugate volcanic rifted margins: $^{40}Ar/^{39}Ar$ chrono-stratigraphy of pre- and syn-rift bimodal flood volcanism in Ethiopia and Yemen. *Earth and Planetary Science Letters*, *198*(3–4), 289–306. https://doi.org/10.1016/S0012-821X(02)00525-3

Vigny, C., Huchon, P., Ruegg, J., Khanbari, K., & Asfaw, L. (2006). Confirmation of Arabia plate slow motion by new GPS data in Yemen. *Journal of Geophysical Research*, *111*, B02402. https://doi.org/10.1029/2004JB003229

Wadge, G., Biggs, J., Lloyd, R., & Kendall, J.-M. (2016). Historical volcanism and the state of stress in the East African Rift system. *Frontiers in Earth Science*, *4*. https://doi.org/10.3389/feart.2016.00086

Wei, S. S., Wiens, D. A., Zha, Y., Plank, T., Webb, S. C., Blackman, D. K., et al. (2015). Seismic evidence of effects of water on melt transport in the Lau back-arc mantle. *Nature*, *518*(7539), 395–398. https://doi.org/10.1038/nature14113

Wessel, P., Smith, W. H. F., Scharroo, R., Luis, J. F., & Wobbe, F. (2013). Generic mapping tools: Improved version released. *Geochemistry, Geophysics, Geosystems*, *94*, 409–410. https://doi.org/10.1002/2013EO450001

Whaler, K. A., & Hautot, S. (2006). The electrical resistivity structure of the crust beneath the northern Main Ethiopian Rift. *Geological Society, London, Special Publications*, *259*(1), 293–305. https://doi.org/10.1144/GSL.SP.2006.259.01.22

White, R. S., & Mckenzie, D. (1989). Magmatism at rift zones: The generation of volcanic continental margins. *Journal of Geophysical Research*, *94*(B6), 7685–7729. https://doi.org/10.1029/JB094iB06p07685

White, R. S., Smith, L. K., Roberts, A. W., Christie, P. A. F., & Kusznir, N. J. (2008). Lower-crustal intrusion on the North Atlantic continental margin. *Nature*, *452*(7186), 460–464. https://doi.org/10.1038/nature06687

WoldeGabriel, G., Aronson, J. L., & Walter, R. C. (1990). Geochronology and rift basin development in the central sector of the Main Ethiopian Rift. *Geological Society of America Bulletin*, *102*(4), 439–458. https://doi.org/10.1130/0016-7606(1990)102<0439:GGARBD>2.3.CO;2

Wolfenden, E., Ebinger, C. J., Yirgu, G., Deino, A., & Ayalew, D. (2004). Evolution of the northern Main Ethiopian Rift: Birth of a triple junction. *Earth and Planetary Science Letters*, *224*(1–2), 213–228. https://doi.org/10.1016/j.epsl.2004.04.022

Wolfenden, E., Ebinger, C. J., Yirgu, G., Renne, P. R., & Kelley, S. P. (2005). Evolution of a volcanic rifted margin: Southern Red Sea, Ethiopia. *Bulletin of the Geological Society of America*, *117*(7), 846–864. https://doi.org/10.1130/B25516.1